



NUCLEAR STRUCTURE OF ^{192}Ir

PROSPECTUS

Trevor W. Warren, Major, USAF

AFIT-ENP-19-M

**DEPARTMENT OF THE AIR FORCE
AIR UNIVERSITY**

AIR FORCE INSTITUTE OF TECHNOLOGY

Wright-Patterson Air Force Base, Ohio

LIMITED DISTRIBUTION

The views expressed in this thesis are those of the author and do not reflect the official policy or position of the United States Air Force, Department of Defense, or the United States Government. This material is declared a work of the U.S. Government and is not subject to copyright protection in the United States.

NUCLEAR STRUCTURE OF ^{192}Ir

PROSPECTUS

Presented to the Faculty

Department of Engineering Physics

Graduate School of Engineering and Management

Air Force Institute of Technology

Air University

Air Education and Training Command

In Partial Fulfillment of the Requirements for the

Doctor of Philosophy in Nuclear Engineering

Trevor W. Warren, MS

Major, USAF

JULY 2017

LIMITED DISTRIBUTION

NUCLEAR STRUCTURE OF ^{192}Ir

Trevor W. Warren, MS

Major, USAF

Approved:

John W. McClory, PhD
Dissertation Advisor

Date

James J. Carroll, PhD
Committee Member

Date

David E. Weeks, PhD
Committee Member

Date

William P. Baker, PhD
Committee Member

Date

I. Contents

II. Introduction	1
Motivation.....	1
Nuclear Data for Basic Research	1
Isomer Energy Storage.....	2
Problem Description and Proposal.....	3
Problem Description	3
Proposal.....	4
Objectives	5
III. Background.....	6
Nuclear Models	6
Independent Particles and the Spherical Shell Model.....	7
Mixing.....	13
The Pairing Interaction and Quasiparticles.....	18
Nuclear Deformity and Collective Motion	22
The Deformed Shell (Nilsson) Model.....	29
The Particle-Plus-Rotor Model	35
Modeling Prolate-Deformed, Odd-Odd Nuclei	40
Nuclear Transitions	45
Quantum Mechanical Treatment.....	45
Lifetimes	46
Electromagnetic Transition Probabilities and Weisskopf Estimates	47
Electromagnetic Transition Selection Rules	48
Internal Conversion.....	50
Gamma Decay Cascades.....	51

Metastable Excited States	53
Nuclear Reactions	56
Definition	56
Classification.....	57
Energetics and Thresholds	58
Cross Sections and Excitation Functions	59
Synopsis of Ir-192 Research	60
NSR, ENSDF, and XUNDL Summary	60
J. Kern et al.	62
P. Garrett et Al.	62
Others	63
Present ENSDF Data and Measurements	63
M. Balodis and T. Krasta (XUNDL)	67
IV. Experiment.....	70
Reactions.....	70
Rationale	70
Predictive Simulations	71
Excitation Function Data	71
Experimental Considerations	72
Accelerator Equipment and Ion Beams	74
14UD Tandem Accelerator	74
Detectors	77
Semiconductor Detectors	77
Spectral Resolution and Efficiency	78
High-Purity Germanium	79

Low Energy Photon Spectrometer	80
Background and Continuum Suppression.....	81
CAESAR Array	82
V. Research Plan.....	83
Objectives	83
Chronology of Events	84
Timetable	86
VII. References.....	87

List of Figures

Figure 1. Binding energy plot showing magic numbers	9
Figure 2. Spherical Shell Model Diagram	11
Figure 3. Illustration of two-state mixing	15
Figure 4. Schematic depiction of mixing	17
Figure 5. Two-state mixing	18
Figure 6. Illustration of partial occupancies due to pairing.	21
Figure 7. Regions of deformity.	23
Figure 8. Nuclear shapes	26
Figure 9. Deformed orbits	31
Figure 10. K -splitting	32
Figure 11. Nilsson Diagram	34
Figure 12. Asymptotic single particle energies of the axially symmetric harmonic oscillator	35

Figure 13. Illustration of the two coupling extremes	37
Figure 14. Deformation aligned and rotation aligned coupling	40
Figure 15. Statistical and yrast cascades	53
Figure 16. Simple pictorial representations for the causes of isomerism	55
Figure 17. Isomer level scheme	56
Figure 18. Subset of the ^{192}Ir adopted level scheme (up to 700 keV)	65
Figure 20. Proposed new positive parity bands for ^{192}Ir .	68
Figure 19. Proposed new negative parity bands for ^{192}Ir .	69
Figure 21. Excitation function data	72
Figure 22. Experimental tradeoffs	73
Figure 23. 14UD tandem accelerator	76
Figure 24. Sample calibration curve for an n-type detector	80
Figure 25. Representative efficiency calibration curves for Si(Li) detectors	81
Figure 26. Schematic diagram of the CAESAR array.	83

List of Tables

Table 1. Comparison of Weisskopf estimates.	48
Table 2. Summary of ^{192}Ir nuclear structure experiments.	61
Table 3. List of ^{192}Ir states with half-lives exceeding one nanosecond.	66

Nuclear Structure of ^{192}Ir

II. Introduction


Iridium-192 is an odd-proton, odd-neutron, radioisotope with a half-life of 73.8 days. It decays either by β^- to ^{192}Pt with a fraction of 95.24% or electron capture to ^{192}Os with a fraction of 4.76% [1]. Nuclides in the transitional region near the 190 isobar are known to exhibit prolate deformation and shape phase transitions associated with proton and neutron counts, which are well removed from the nearest magic numbers at 82 and 126, respectively [2, 3]. Coupled with the odd-odd nature of the nucleon quantities, this results in complex structure and dynamical behavior, which is poorly understood. As a consequence of such structure, ^{192}Ir plays host to known metastable (isomeric) states, with the 168 keV (m2) isomer of particular interest due to its long 241-year half-life, as specified in [1]. Should a suitable mechanism for depletion of the m2 isomer be identified, ^{192}Ir could find practical application as an energy storage medium. Collectively, the structural properties of ^{192}Ir make it a valuable target for experimental research.

Motivation

This research aims to address for the U.S. Department of Energy, outstanding requirements of the Nuclear Data Program; and for the U.S. Department of Defense, outstanding requirements of the Army Research Laboratory (ARL) Directorate of Electron Devices.

Nuclear Data for Basic Research


The executive body for the U.S. Department of Energy Nuclear Data program is the National Nuclear Data Center (NNDC) at Brookhaven National Laboratory in Upton, NY. NNDC maintains there is a significant and continuous demand for current, evaluated nuclear structure and reaction data [NNDC website]. Compilation and maintenance of such data in the Evaluated Nuclear Structure Data File (ENSDF) database are vital for continued progress in nuclear science [4]. NNDC also identifies the following specific areas of research, which benefit directly from the ENSDF data: nuclear structure, nuclear reactions, nuclear astrophysics, nuclear theory, and neutrino science. It is the expectation of the author the present research will contribute substantively to nuclear structure, and nuclear theory.

With respect to nuclear structure, the particular set of proposed experiments should enable exploration of nuclear spin states  for which little data exists. Excepting the m2 isomer, the ENSDF data indicate the highest observed angular momentum in the ^{192}Ir level scheme is tentatively $6\hbar$. The new data will also enable improvement to the existing level scheme through the identification of unknown transitions and confirmation of tentative spin-parity assignments.

Contribution to nuclear theory will be manifest as measurements, which facilitate calculation of nuclear model parameters and values for the physical observables the models predict. Subsequent comparison of the modeled spectra and level schemes with those determined through experiment should enable revisions to the model(s). This is particularly important for odd-odd deformed nuclei, whose structural complexities lend considerable difficulty to modeling [5].

Isomer Energy Storage

The utility of portable power sources having high energy storage density (energy per unit mass) is practically axiomatic. With energy trapped in metastable radioisotope nuclei, an isomer energy storage medium could achieve an energy density five to six orders of magnitude greater than present chemical storage technology as well as theoretical specific power (power per unit mass) at parity with present technology [6, 7]. Given that Special Forces soldiers must regularly carry nearly forty pounds of batteries into the field [6] and launch costs for spacecraft are in excess of ten thousand dollars per pound, it is clear the DoD could make use of such technology, should it exist. Indeed, a vast array of defense and commercial applications is conceivable.

The concept behind an isomer power source is relatively simple, in theory. As an isomer, a nucleus is effectively “trapped” in a local energy well, whose minimum is above that of the true ground state. One may “free” the trapped nucleus by supplying sufficient energy to excite it from the metastable, isomeric state into a higher excited state, which has an unhindered decay path to the true ground state. This process is loosely analogous to overcoming the activation barrier in a chemical reaction. Accordingly, so long as the sum of the recoverable isomeric and beta decay energies exceed the energy of activation, the net output is positive. In the case of ^{192}Ir , the isomer lies at 168 keV while the ground state decay proceeds via  emission with a frequency of 95%, releasing an average of 1450 keV in the process [1]. The beta energy is then available for harvest

using a semiconductor, scintillator, or related betavoltaic technology. Furthermore, the ^{192}Ir decay yields stable ^{192}Pt (95%) and stable ^{192}Os (5%), thus leaving no radioactive waste.

However, while the theory is straightforward, demand depletion of the isomer is more difficult in practice. Realization of positive energy balance, following the depletion process, requires precise tuning of the excitation source into resonance with the energy gap which separates the isomer from its decay path to the ground state. The proper resonance maximizes the cross section for excitation of the nucleus out of the metastable state, thereby limiting the required input energy. Thus, the identification of a precise pathway to depletion is required for a viable isomer power source; and such a path can only be determined through detailed structural knowledge of the nucleus. Naturally then, design of experiments to test concepts for activation and/or depletion of the $^{192}\text{m}2$ isomer requires detailed knowledge of the ^{192}Ir level structure, which this research intends to provide.

Problem Description and Proposal

Problem Description

Present data in the ENSDF lists a significant majority of spin-parity assignments for the ^{192}Ir level scheme as tentative. Currently residing in the Experimental Unevaluated Nuclear Data List (XUNDL) is a manuscript detailing reanalysis of this existing, evaluated data by Balodis et al; it reports confirmation (or confident revision) for most of the tentative assignments in the ENSDF [8]. However, the authors also propose, as an addition to the evaluated level scheme, several new, tentative levels. A more recent conference publication by the same authors also suggests the need for additional experimental measurements, particularly those such as gamma coincidence, which are sensitive to collective core excitations [3]. Moreover, most of the gamma observations used in the development of these level schemes originated with low angular momentum ($<7\hbar$) excitation, accessed via radiative neutron capture reactions on ^{191}Ir . Observation of decays from higher angular momentum states could make available further additions to the level scheme, identification of a possible depletion path for the (11^-) m2 isomer, and valuable insight into high-spin behavior of complex nuclei. Accordingly, the work of T. Bengtsson suggests there exists significant benefit in the use of gamma coincidence for deduction of collective dynamics at high angular momentum [9]. Thus, with specific deficiencies in the existing body of ^{192}Ir structure

data, and generally shallow understanding of complex structure in odd-odd, deformed nuclei, additional experimental measurements of ^{192}Ir are warranted, particularly using gamma coincidence techniques.

Proposal

Beginning in late 2017, the ^{192}Ir research campaign will run for one to two years and encompass three phases of experimentation, each employing a different, ion-induced reaction to explore the space of ^{192}Ir angular momentum and energy excitation. All experiments will take place in the Heavy Ion Accelerator Facility (HIAF) at the Australian National University (ANU), in Canberra, Australia. The HIAF possesses equipment and instrumentation well suited to the requirements for spectroscopic investigations of odd-odd nuclei and nuclear isomers [10, 11]. The sequential execution of all experiments at a single facility is advantageous for progressive refinement of individual experiment parameters as the research campaign unfolds; and, consequently, the specific phase sequence is deliberate [10, 11].


The first experiment phase will employ a deuteron beam incident on a ^{192}Os target. The placement of this experiment first in the campaign is based on the expectation it should provide a survey of the ^{192}Ir level structure at moderate angular momentum [10, 11]. Recent analysis of a similar experiment on ^{187}Re suggests this will be the case [12].

A second phase involves a ^7Li beam. This reaction should impart significant angular momentum to the ^{192}Ir product, enabling access to states above the (11^-) m2 isomer [10, 11]. Note, according to the present NNDC dataset (both evaluated and unevaluated) for the ^{192}Ir nucleus, no experimental work to date has explored angular momentum excitation of this magnitude [1].


The third and final phase of experimentation uses a proton beam. While this reaction may excite only relatively low angular momentum states, these can serve to inform the analyses of the other experiments [10, 11].

Accelerator equipment at the HIAF includes the electrostatic 14UD Tandem Accelerator (Pelletron), which serves as the primary source for seven beamlines as well as the injector for three beamlines feeding a second linear accelerator. The 14UD is capable of operating at electrostatic potentials in excess of 15 MV. Beam control apparatus includes a programmable

chopper, buncher, and harmonics, which collectively shape the ion pulses to sub-nanosecond widths at repetition rates ranging from sub-microseconds to multi-milliseconds [12]. For each experiment, these accelerators supply the requisite ion beams, with beam parameters tailored for optimum measurement sensitivity [10, 11].

The primary detection instrument is the CAESAR gamma spectrometer array, which consists of eleven high-purity germanium (HPGe) detectors (four mpton suppressed) and two low-energy photon spectrometer (LEPS) detectors distributed around the target [10, 11, 13]. In total, the combined designs of CAESAR and the accelerator system permit measurements of low-energy transitions, coincidences between beam bursts, and temporal correlations across long-lived states – all crucial to the study of odd-odd nuclei and isomers [9, 10, 11].

Gamma radiation events, which CAESAR detects, are composed (sorted), based on the time interval between detections, into two-dimensional (γ - γ) and possibly three-dimensional (γ - γ - γ) coincidence histogram arrays. Analyses of the singles, γ - γ , and γ - γ - γ spectra are conducted, respectively, using the *gf3*, *escl8r*, and *levit8r* programs in the software suite *RadWare*, which is available through the Oak Ridge National Laboratory [61]. The output of the spectral analysis is a ^{192}Ir level scheme capturing the observed gamma transition energies, deduced levels with spin-parity assignments, and deduced transition branching ratios. The level scheme is then interpreted in terms of phenomenological model predictions, such as rotational banding. Specific details about the isomer(s), including feeding and possible depletion pathways emerge, inherently, in the level scheme results. Additionally, information derived from the level scheme may facilitate calculations of theoretical model parameters and physical observables, which provide valuable tests of the models.

Each experiment should produce adequate data and analysis for at least one peer reviewed publication in a professional, refereed journal. Additionally, one could y these journal publications to serve as proceedings at professional conferences, if desired.

Objectives

Explicit objectives of this research include:

- Addition, to the existing ^{192}Ir level scheme in the ENSDF, transitions with spin-parity assignments, and phenomenological features of nuclear structure
- Confirmation of tentative transitions, spin-parity assignments, and phenomenological features
- Identification of feeding and decay pathways for the m2 isomer, to facilitate future experimentation and practical application

III. Background

Proper appreciation for this research and its motivation demands familiarity with the existing body of knowledge describing ^{192}Ir . In particular, this includes the collective set of measurements which presently exist for this nucleus, and the theoretical models employed to explain them. Additionally, some familiarity with the present knowledge of similar nuclei may be beneficial.

Nuclear Models

Nuclear models, which seek a detailed quantum mechanical description of nuclear structure, are typically applicable up to several MeV above the ground state [33]. Beyond this range, the nuclear level density is such that quantum mechanical treatments give way to those of statistical mechanics, which employ bulk properties of nuclear matter [33]; and nuclear spectra lose their discrete structure, becoming unresolvable with present spectroscopic techniques. Consequently, the experimental and theoretical foci of this research lie with the lower energies, where spectroscopic measurements are explicable in a quantum mechanical framework.

Unfortunately, even at the lower energies, a precise and pedagogical treatment of nuclear structure is elusive, owing to the uncertain nature of the nucleon-nucleon interaction, for which a derivation from first-principles does not yet exist [33]. This difficulty gives rise to several different approaches for modeling nuclei. Most generally, there are (1) the microscopic models, which attempt to reproduce experimental data through parameterized nucleon-nucleon interactions, based on a speculative functional form; and (2) the macroscopic models, which rely on degrees of freedom referring to bulk nuclear properties, instead of individual nucleons [33]. In terms of pedigree, the former are descendants of the spherical shell model, whereas the latter

evolved from the collective model of Bohr and Mottelson [34]. In modern methodologies, it is common to employ hybridized models, which may combine elements of both. For nuclei, such as ^{192}Ir , which are deformed and doubly odd in terms of their proton and neutron numbers, the presently-favored approach emphasizes a microscopic description, employing certain collective dynamics (i.e. rotation).

Independent Particles and the Spherical Shell Model

One might consider the spherical shell model, often truncated to “shell model”, as fundamental in the landscape of nuclear models [34]. Its foundation is the independent particle approximation, which seeks to explain the structure of the nucleus in terms of independent nucleons, collectively generating and freely moving in a central potential. In the extreme case, or extreme independent particle approximation, such structure is the consequence of a single exterior or valence nucleon interacting with the potential well, which an inner core of inner nucleons generates [35].

As a most general point of departure for modeling the nucleus, one may begin by defining a Hamiltonian H , in terms of the collective kinetic energy T , for all particles, and the collective inter-particle potential U , such that

$$H = T + U = \sum_{i=1}^A \frac{\mathbf{p}_i^2}{2m_i} + \sum_{i>k=1}^A U_{ik}(\mathbf{r}_i - \mathbf{r}_k), \quad (1)$$

where A is the number of nucleons in the nucleus [35]. Ideally, solution of the time-independent Schrodinger equation

$$H\psi_i = E_i\psi_i, \quad (2)$$

would then yield the basis states ψ and energy eigenvalues E for each of the i particles in the nuclear system. However, complexity arising from the many-body interaction U , which requires $3A$ position coordinates, invites a mean field approximation [35] to reduce the dimensionality of the problem. With a mean field potential given by

$$\sum_k \int \psi_k^*(\mathbf{r}) U_{ik}(\mathbf{r}_i - \mathbf{r}_k) \psi_k(\mathbf{r}) d\mathbf{r}, \quad (3)$$

it is common to proceed via a Hartree-Fock approach, whereby one posits a guess for ψ to calculate the mean field potential, then uses the new potential to recalculate ψ , and subsequently iterates in this fashion until achieving self-consistent convergence [34].

Instead, as an alternative to the Hartree-Fock calculations, tremendous simplification results from *choosing* a central, mean field potential, which reproduces the empirical natures of both the nuclear potential well and nuclear shell structure. This is the origin of the spherical shell model. Importantly, the primary consideration, in terms of adequate nuclear structure facsimile, is prediction of the observed magic numbers [33]:

$$2, 8, 20, 28, 50, 82, 126. \quad (4)$$

Nuclei, having nucleons of either species in one of these quantities, are characterized by [33, 34]:

- a larger total binding energy, relative to surrounding nuclei,
- a substantial decrease in the energy required to separate nucleon $i+1$ of a particular species, relative to nucleon i of the same species, where i is a magic number
- a higher energy of the lowest excited states relative to neighboring nuclei, and
- a large number of isotopes (isotones) with the same magic number for protons (neutrons).

In terms of total nuclear binding energies, the magic numbers result in the appearance of the “islands” around local maxima, depicted in Figure 1

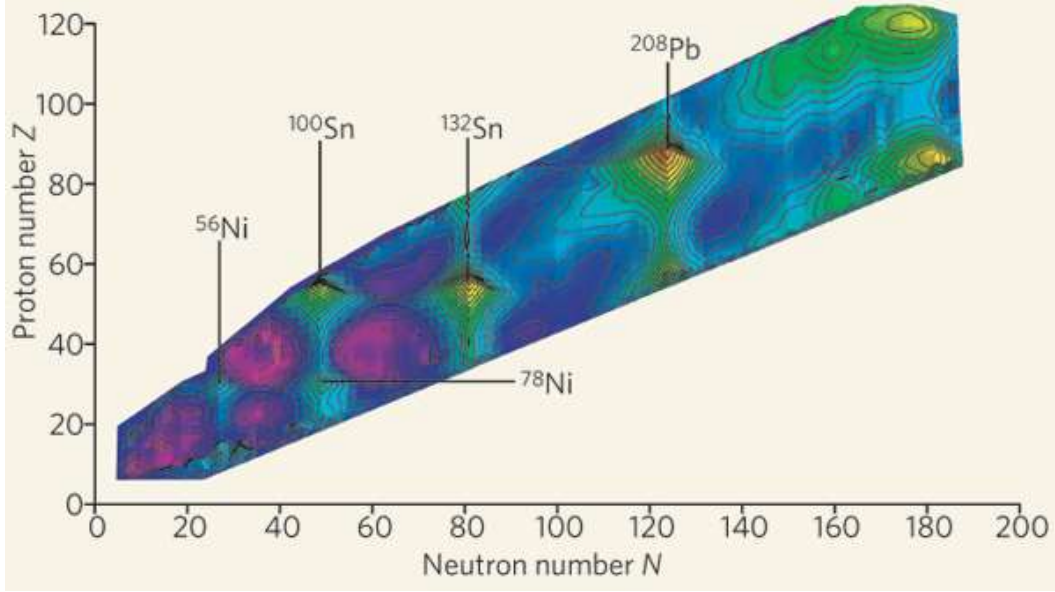


Figure 1. Plot depicting, as a function of proton and neutron number, the binding energies of the nuclides, with the color scale ranging from violet (lowest) to red (highest) [36, 37]. “Islands” of high total binding energy appear in the vicinity of magic numbers for both protons and neutrons. Coulomb repulsion of the protons, which lowers the total binding energy, is the reason why the islands do not, in general, appear at the intersections of proton and neutron magic numbers.

Construction of a suitable central, mean field potential V may begin with a variety of forms including (but not limited to) [33]:

- the Woods-Saxon potential [33, 38]

$$V(r) = -\frac{V_0}{1 + \exp(r - R)/a} \quad (5)$$

with well depth V_0 , nuclear radius R , and surface thickness a ,

- the harmonic oscillator

$$V(r) = \frac{1}{2}m\omega^2r^2 \quad (6)$$

with oscillator frequency ω , or

- the square well

$$V(r) = \begin{cases} -V_0, & r \leq R \\ \infty, & r > R \end{cases} \quad (7)$$

Each of these forms has distinct advantages and disadvantages in its representation of the nuclear well and its practical tractability. The harmonic oscillator, being analytically convenient, is a popular choice. However, as it tends to infinity at large distances, it fails to replicate precisely the empirical nature of the nuclear potential, which falls to zero [33]. Nevertheless with appropriate modification, the harmonic oscillator demonstrates reasonable predictive capacity for nuclear structure phenomena.

In particular, the crucial modification, which Mayer, Haxel, Jensen, and Suess introduce in 1948 [33, 39], is the addition of a spin-orbit coupling term

$$V_{ls} = -V_{ls} \frac{\partial V(r)}{\partial(r)} l \cdot s \quad (8)$$

where

$$l \cdot s = \frac{\hbar^2}{2} (j(j+1) - l(l+1) - s(s+1)), \quad (9)$$

and

$$j = l + s \quad (10)$$

with strength constant V_{ls} , orbital angular momentum projection l , and intrinsic spin projection s .

A second modification includes a centrifugal term in l^2 to flatten the harmonic oscillator well, bringing it closer to the Woods-Saxon form, which gives better agreement with empirical data but is more analytically challenging [34]. Due to the central nature of the potential in the Hamiltonian, the Schrodinger equation is separable, such that $\psi(r, \theta, \varphi) = R(r)\Theta(\theta)\Phi(\varphi)$, yielding the respective component equations in polar angle, azimuthal angle, and radius [34, 35]:

$$\frac{d^2\Phi}{d\varphi^2} + m_l^2\Phi = 0 \quad (11)$$

$$\frac{1}{\sin\theta} \frac{d}{d\theta} \left(\sin\theta \frac{d\Theta}{d\theta} \right) + \left(l(l+1) - \frac{m_l^2}{\sin^2\theta} \right) \Theta = 0 \quad (12)$$

$$\frac{\hbar^2}{2m} \frac{d^2 R}{dr^2} + \left(E - V(r) - \frac{\hbar^2}{2m} \frac{l(l+1)}{r^2} \right) R = 0 \quad (13)$$

Respective solutions for the angular and radial equations are the spherical harmonics $Y_{lm}(\theta, \varphi)$ and the Laguerre polynomials in r^2 . The diagram in Figure 2 schematically illustrates the resulting energy eigenstates, which one traditionally labels according to the spectroscopic notation $l = \{0, 1, 2, 3, 4, 5, \dots\} : \{s, p, d, f, g, h, \dots\}$. The fractional value indicates $j = l + s$ ($= l \pm 1/2$).

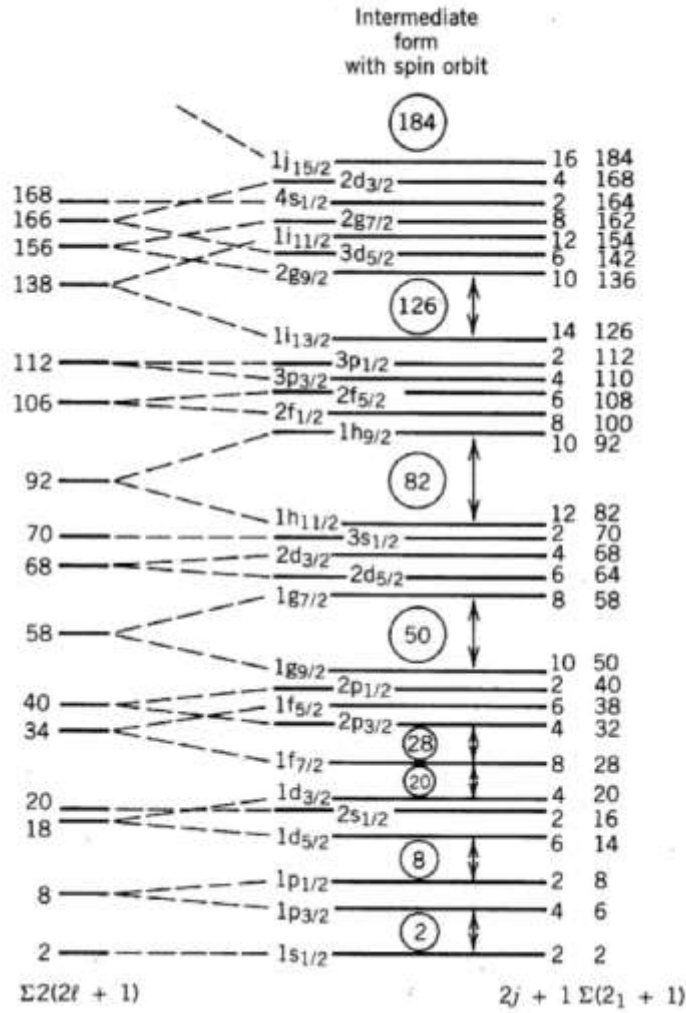


Figure 2. Diagram of spherical shell model eigenstates, which result from the harmonic oscillator potential, combined with a centrifugal (l^2) potential and spin-orbit interaction. The far right column gives the cumulative nucleon quantity ($\Sigma(2j+1)$) at a particular level, whereas the column immediately to the left indicates the $2j+1$ degeneracy of the level. The letters in the central column indicate the nucleon angular momentum, according to traditional spectroscopic notation (i.e. $l = \{0, 1, 2, 3, 4, 5, \dots\} : \{s, p, d, f, g, h, \dots\}$), and the fraction indicates the alignment of the nucleon intrinsic spin ($\pm 1/2$). It is evident the magic numbers are present at the large energy gaps in the level structure, consistent with empirical observations. Reproduced from [35]

Due to the spin-orbit interaction, the state, formed by the alignment of s with a given l , exists lower in the potential well than the state formed by antialignment; and the ensuing level arrangement nicely reproduces the energy gaps associated with the magic numbers. The existence of spherical symmetry in the system ensures the $2l+1$ subspace of the spherical harmonics, which determine the angular distributions of the nucleon orbits, is degenerate. As a consequence of the Pauli exclusion principle, each degenerate state, or magnetic substate m_j , can contain one nucleon of each species, giving a total degeneracy of $2(2j+1)$. Beginning with the lowest $s_{1/2}$ state, nucleons successively fill the level structure, occupying each m_j substate in a given level, before continuing to the next. A nucleon's position in the level structure determines its single-particle energy, angular momentum j , and parity π , where

$$\pi = (-1)^l. \quad (14)$$

In general, the total nuclear angular momentum J is the sum of the single particle angular momenta, according to

$$J = \sum_i j_i, \quad (15)$$

and the nuclear parity is the product of the single particle parities, according to

$$\pi = \prod_i \pi_i, \quad (16)$$

collectively giving a nuclear spin-parity assignment, denoted J^π .

However, by spherical symmetry, filled m_j subspaces (minor shells) can contribute nothing to the total angular momentum; and, moreover, nucleons of a particular species tend to form pairs, whose total angular momentum couples to zero. It is evident, then, the ground state spin-parity of an odd- A nucleus is the single-particle spin-parity of the valence, unpaired nucleon, whereas that of a nucleus, with even numbers of both species (even-even) must be $J^\pi = 0^+$, due to pairing. In the case where the nucleus contains an odd number of each species (odd-odd) the ground state dynamic is more complex and not in general predictable using the spherical shell model. One handles excitation in the shell model by promotion of nucleons in the level structure, often with

considerations for the destruction and creation of nucleon pairs.

Mixing

Physically, the picture of the shell model is incomplete in that its potential is an approximation and not a perfect representation of the many-body nuclear interaction. Ultimately, this limits the shell model's descriptive capability. However, to some extent, one can overcome this limitation by mixing the shell states with residual interactions, which create a small perturbation to the original Hamiltonian. This process is divisible into two components: the application of perturbation theory and the choice of a suitable perturbing interaction for the problem at hand.

General treatment of a perturbed system involves decomposition of the Hamiltonian into a component H_0 , whose eigenfunctions ϕ and eigenvalues ε are known, as well as a perturbing term H' , which is small relative to H_0 [40]. This results in the Schrodinger equation

$$(H_0 + \lambda H')\psi_n = E_n \psi_n, \quad (17)$$

where λ is an infinitesimal parameter, owing to the smallness of H' . To first order in λ , and in the case of non-degenerate ε ,

$$\psi_n = \phi_n + \lambda \phi'_n \quad (18)$$

and

$$E_n = \varepsilon_n + \lambda \varepsilon'_n. \quad (19)$$

With the condition that expansion terms in any order of λ must independently vanish, substitution of (18) and (19) into (17), gives the relation

$$(H_0 - \varepsilon_n)\phi'_n = (\varepsilon'_n - H')\phi_n. \quad (20)$$

The action of H_0 on ϕ' suggests

$$\phi'_n = \sum_j c_{nj} \phi_j. \quad (21)$$

Now, substitution of (21) into (20) and use of the orthogonality relations for the ϕ_n , gives

$$(\varepsilon_i - \varepsilon_n)c_{ni} + H'_{in} = \varepsilon'_n \delta_{in} , \quad (22)$$

where

$$H'_{in} = \langle \varphi_i | H' | \varphi_n \rangle \quad (23)$$

are the matrix elements of H' in the φ basis. Thus, for $i \neq n$, the coefficients c_{ni} and the first order corrections to the φ_n are

$$c_{ni} = \frac{H'_{in}}{\varepsilon_n - \varepsilon_i} , \quad (24)$$

$$\varphi'_n = \sum_{i \neq n} \frac{H'_{in}}{\varepsilon_n - \varepsilon_i} \varphi_i , \quad (25)$$

with $c_{nn} = 0$ by the implicit orthogonality of the φ' and φ basis elements [40]. For $i = n$, the first-order corrections to the ε_n are [40]

$$\varepsilon'_n = H'_{nn} . \quad (26)$$

In the case where states mix through perturbing interaction H' , one may proceed by solution of the eigenvalue problem

$$\begin{pmatrix} \varepsilon_1 & H'_{12} & \dots & H'_{1n} \\ H'_{21} & \varepsilon_2 & & \vdots \\ \vdots & & \ddots & \vdots \\ H'_{i1} & \dots & \dots & \varepsilon_i \end{pmatrix} \begin{pmatrix} c_{1n} \\ \vdots \\ c_{in} \end{pmatrix} = E_n \begin{pmatrix} c_{1n} \\ \vdots \\ c_{in} \end{pmatrix} \quad (27)$$

or

$$\begin{vmatrix} \varepsilon_1 - E & H'_{12} & \dots & H'_{1n} \\ H'_{21} & \varepsilon_2 - E & & \vdots \\ \vdots & & \ddots & \vdots \\ H'_{i1} & \dots & \dots & \varepsilon_i - E \end{vmatrix} = 0 \quad (28)$$

in the φ basis [34, 41, 42].

A simple case is a system with two states, which mix through interaction H' . Determination of the new energies and wave functions requires diagonalization of the 2×2 matrix

$$\begin{pmatrix} \varepsilon_1 - E & V \\ V & \varepsilon_2 - E \end{pmatrix}, \quad (29)$$

where V is the mixing matrix element, defined according to (23); and Roman numeral subscripts denote the results of the mixture. Figure 3 schematically depicts this interaction, termed two-state mixing.

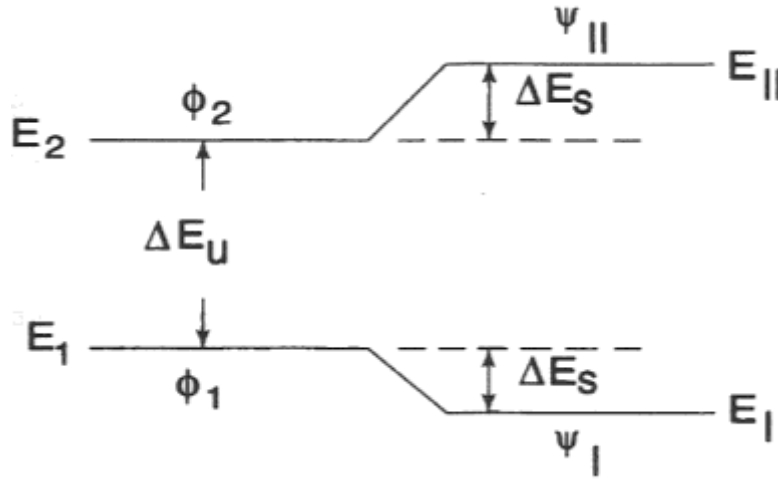


Figure 3. Illustration of two-state mixing. Reproduced from [34].

It is convenient, for generalization of the two-state mixing results, to define the mixing ratio R involving the difference of the unperturbed energies $\Delta E_u = |\varepsilon_2 - \varepsilon_1|$ and the mixing element, such that

$$R = \frac{\Delta E_u}{V}. \quad (30)$$

With this definition, a universal expression, for the energy shift $|\Delta E_s|$ of the unperturbed E_u due to V , becomes

$$|\Delta E_s| = \frac{\Delta E_u}{2} \left(\left(1 + \frac{4}{R^2} \right)^{1/2} - 1 \right), \quad (31)$$

which is completely independent of V [34]. In terms of units in ΔE_u , this is

$$|\Delta E_s| = \frac{1}{2} \left(\left(1 + \frac{4}{R^2} \right)^{1/2} - 1 \right), \quad (32)$$

which is also independent of the initial spacing between the E_u . The mixed wave functions are then

$$\psi_I = \alpha \varphi_1 + \beta \varphi_2, \quad (33)$$

and

$$\psi_{II} = -\beta \varphi_1 + \alpha \varphi_2. \quad (34)$$

with

$$\alpha^2 + \beta^2 = 1, \quad (35)$$

and the mixing amplitude

$$\beta = \frac{1}{\sqrt{1 + \left(R/2 + \sqrt{1 + R^2/4} \right)^2}}. \quad (36)$$

Limiting cases of two-state mixing include degenerate states, for which the mixing is complete ($\beta = \alpha = \sqrt{2}$) and a weak mixing limit, in which $R \ll 1$. These are illustrated in Figure 4 [34]. When the initial states are degenerate, (31) is clearly no longer valid. However, with the intermediate result

$$E_{I,II} = \frac{E_1 + E_2 \mp \sqrt{(E_2 - E_1)^2 + 4V^2}}{2} \quad (37)$$

(I corresponding to “-“ and II to “+”), it is evident [34]

$$E_{I,II} = \frac{1}{2} \left((E_1 + E_2) \mp 2V \right) = E_0 \mp V, \quad (38)$$

lifting the degeneracy by twice the magnitude of the mixing element. Thus, as a general consequence of two-state mixing, the final separation for an isolated two-state system can never be less than twice the mixing magnitude [34].

In the case of weak mixing, $\beta \rightarrow 1/R$ by equation (36), giving

$$V \approx \beta \Delta E_u \approx \beta \Delta E_{I,II}, \quad (39)$$

a useful relationship for deducing V from empirical data.



Figure 4. Schematic depiction of strong mixing from two initially degenerate states (left) and weak mixing from two initially distinct, highly separated states (right). Reproduced from [34].

If the E_u of the two-state system are dependent on a nuclear structure parameter x , the mixing will inherently be a function of x as well. At the point of closest approach in x , the minimum separation of the two states, corresponding to equal admixtures of both, must be $2V$ according to (38). Thus there exists an inflection point, at which one may derive the magnitude of the mixing element by inspection [34]. On either side of the inflection point, the wave function of one state takes on a larger amplitude for the wave function of the opposite parent state. This situation, as depicted in Figure 5, is broadly applicable in nuclear structure and, in particular, reflects interactions of nucleon orbits in the Nilsson model, where x represents the nuclear density.

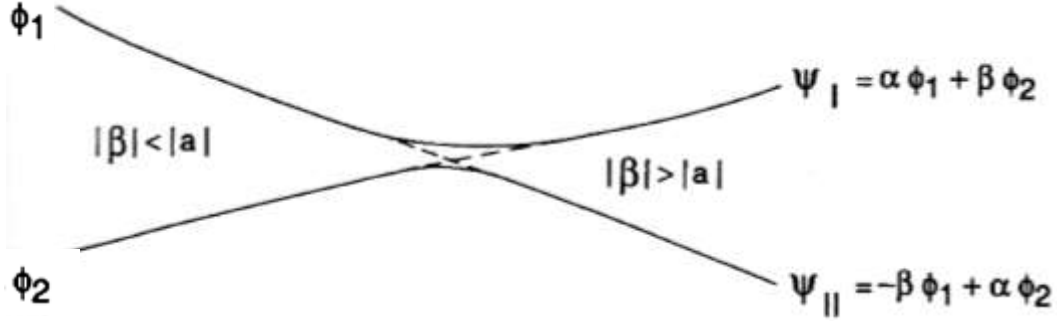


Figure 5. Schematic diagram showing variation of a two-state admixture with an arbitrary parameter. Reproduced from [34].

Mixing for systems involving more than two states is generally of greater complexity and requires explicit diagonalization of the perturbation matrix (28). However, in a few special cases, generic results emerge [34].

- Case 1: a system with N initially degenerate levels and a constant mixing element (i.e. each pair of states mixes equally). The mixed system will include one level, which is lowered by $(N - 1)V$, whereas the rest are raised by one unit of V .
- Case 2: a system with N equally spaced levels and a constant mixing element. One state is again lowered as in (Case 1) but the ratio of the non-degenerate lowering to the degenerate lowering is nearly independent of N for a given R . Thus, for degenerate (D) and non-degenerate (ND) circumstances, one can approximate the multi-state lowering, using the two-state result, according to

$$\frac{[\Delta E_{ND}]_{N\text{-state}}}{(N - 1)V} = \frac{[\Delta E_{ND}]_{2\text{-state}}}{[\Delta E_D]_{2\text{-state}}} = \left[\frac{\Delta E_s}{V} \right]_R. \quad (40)$$

- Case 3: a system with N closely-spaced levels, which only mix with adjacent levels. As an idealization, one considers the level spacing to be infinitesimal – a limit, which is not distant from the real phenomenon of Coriolis mixing among a series of bands in heavy nuclei [34]. Under this circumstance, the mixed levels are symmetrically distributed above and below the initial (approximately degenerate) level.

The Pairing Interaction and Quasiparticles

Motivating the need for this perturbation and mixing apparatus are experimental observations, which are not immediately explicable in the shell model; these invite the development of various

interactions both microscopic (particle to particle) and collective. Among the microscopic interactions, the pairing correlation, in particular, enjoys wide adoption for its utilitarian explanation of several empirical phenomena, including [34]:

- The $J^\pi = 0^+$ ground state of all even-even nuclei
- The “pairing gap” arising from 0^+ states, which normally lie far below the next intrinsic states
- A binding energy for even-even nuclei, about one to two MeV higher than their odd-A neighbors
- A sharp rather than smooth transition from spherical to aspherical forms as nuclei depart from closed shells – suggestive of a force, which favors a sphere
- Empirical moments of inertia, systematically lower than those based on the shell model
- Higher than expected density of Nilsson orbit distributions near the ground states of odd-A nuclei

Qualitatively, the pairing interaction is a strong, short-range attraction between identical nucleons, which have wave functions with high spatial overlap [34]. The matrix elements determine the precise definition according to

$$\langle j_1 j_2 J | V_{pair} | j_3 j_4 J' \rangle = -G \sqrt{\left(j_1 + \frac{1}{2}\right) \left(j_3 + \frac{1}{2}\right)} \delta_{j_1 j_2} \delta_{j_3 j_4} \delta_{J_0 J'_0} , \quad (41)$$

with strength constant G . Of particular note are the following attributes of the interaction:

- It is independent of magnetic substate but scales with the $2j+1$ degeneracy of an orbital shell
- G decreases with A in heavier nuclei due to reduced spatial overlap as nucleon orbits get farther apart
- As a consequence of the Coulomb interaction between protons, G has different magnitudes for protons and neutrons, with respective values typically taken to be (in MeV) $17/A$ and $23/A$
- The diagonal and off-diagonal (mixing) matrix elements are equally strong

Intuitively, the pairing interaction couples to 0^+ , the angular momenta between two nucleons in the same j state. While this picture is correct, the strong, off-diagonal matrix elements linking j^2 and j'^2 states also enable “scattering” of pairs, with scattering amplitudes determined according to (41), such that

$$\frac{\langle j^2 J = 0 | V_{pair} | j'^2 J = 0 \rangle}{(\varepsilon_j - \varepsilon_{j'})} = \frac{G}{(\varepsilon_j - \varepsilon_{j'})}. \quad (42)$$

This has the effect of building among the pair wave functions a coherence, which further lowers the lowest 0^+ state [34]. Ordinarily, in the absence of pairing, the nucleus would sequentially occupy, based on the Pauli principle, each available level up to the Fermi energy or Fermi surface. However, mixing of the 0^+ states enables occupation of levels above the Fermi surface, thus creating partial occupancies above and below. Such partial occupancies, also alter the conceptual role of hole excitations [34].

To explicitly model these phenomena one typically defines the gap parameter Δ as a sum over the orbits i, j according to

$$\Delta = G \sum_{i,j} U_i V_j. \quad (43)$$

Defining the Fermi surface λ , the quantities U and V give the emptiness and fullness factors, or respectively, the probabilities that orbit i with energy ε_i is empty and full, according to

$$U_i = \sqrt{\frac{1}{2} + \frac{(\varepsilon_i - \lambda)}{2\sqrt{(\varepsilon_i - \lambda)^2 + \Delta^2}}}, \quad (44)$$

$$V_i = \sqrt{\frac{1}{2} - \frac{(\varepsilon_i - \lambda)}{2\sqrt{(\varepsilon_i - \lambda)^2 + \Delta^2}}}, \quad (45)$$

with

$$U^2 + V^2 = 1. \quad (46)$$

Noting the behavior of V^2 with respect to $(\varepsilon_i - \lambda)/\Delta$, as Figure 6 depicts, it is evident pairing introduces a smoothing effect for occupancy near the Fermi surface [34]. The smoothing is inversely related to the interaction strength G , which is directly proportional to Δ .

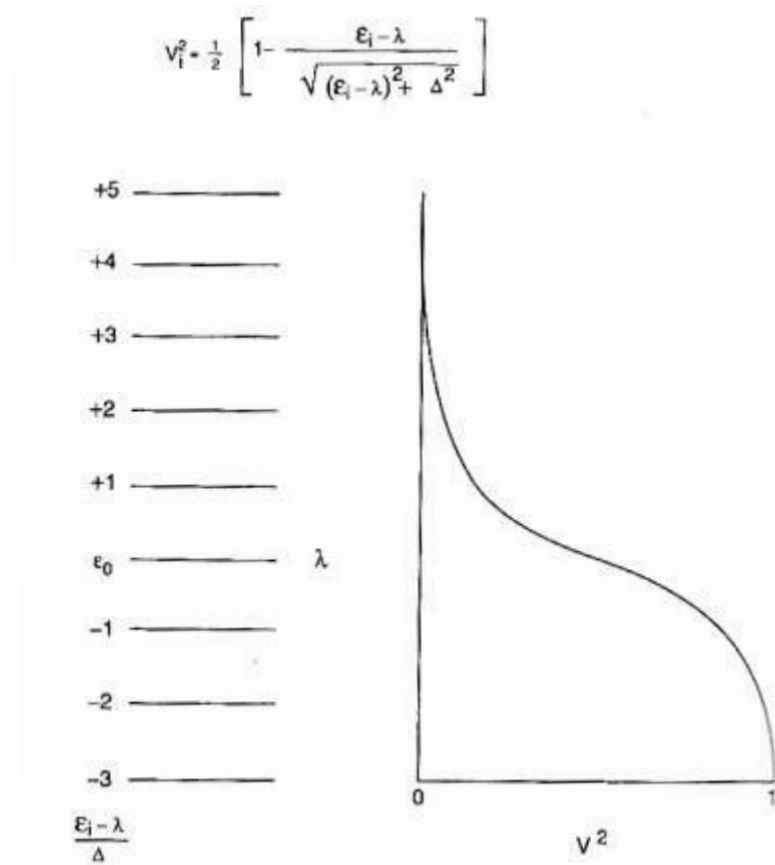


Figure 6. Illustration of partial occupancies due to pairing. Reproduced from [34]

Without pairing, the Fermi surface represents the highest occupied level; then the quantity $(\varepsilon_i - \lambda)$ gives the single-particle excitation energy necessary for a particle at the Fermi surface to reach energy ε_i . Pairing, however, clearly has an effect on the ground state and excitation systematics. Accordingly, quasiparticles, representing partially filled states, replace single particles and vacancies. The excitation energy then becomes the quasiparticle excitation energy

$$E_i = \sqrt{(\varepsilon_i - \lambda)^2 + \Delta^2}, \quad (47)$$

in place of the single-particle value. One now can define excitation in terms of creation and annihilation of quasiparticles – a paradigm, which introduces significant simplification compared to shell model [34]. Therein, one must consider the many permutations of a particular J state in a

major shell, as well as complex scattering wave functions. Alternatively, the quasiparticle formulation treats excitation in the vicinity of Δ at the Fermi surface; and the complexity of partial level occupancy assumes a statistical representation in the quasiparticle ground state [34].

Whereas Δ is the minimum quasiparticle energy, as evident in (47), it does not represent the true ground state. Instead, for an odd-A nucleus one must define the ground state using the single particle level ε_0 nearest the Fermi surface. The excitation energy then becomes

$$[\chi_i]_O = E_i - E_0 = \sqrt{(\varepsilon_i - \lambda)^2 + \Delta^2} - \sqrt{(\varepsilon_0 - \lambda)^2 + \Delta^2}, \quad (48)$$

which has the effects of (1) decreasing excitation energies and compressing the spectrum for $(\varepsilon_i - \lambda) \ll \Delta$; and (2) decreasing all excitation energies by Δ for $(\varepsilon_i - \lambda) \gg \Delta$.

When treating an even-even nucleus, the lowest excitation corresponds to the separation of a pair and promotion of one nucleon to a higher orbit. Thus it is a two-quasiparticle excitation, one each for the excited nucleon and the new vacancy, which determines the energy

$$[\chi_{in}]_{EE} = \sqrt{(\varepsilon_i - \lambda)^2 + \Delta^2} + \sqrt{(\varepsilon_n - \lambda)^2 + \Delta^2}. \quad (49)$$

In the limit both single-particle/hole excitation energies lie on the Fermi surface, the minimum energy of the first excited state corresponds to the pair separation energy. Clearly this is 2Δ , giving the even-even pairing gap, as expected. An empirical determination of Δ is thus possible through measurement of the energy difference.

Generally speaking, the pairing interaction is significant to the structure of heavy nuclei. It modifies most nuclear matrix elements and influences microscopic structure of collective excitations [34]. It also serves as the basis for the quasiparticle picture, frequently used in the theoretical descriptions of heavy, deformed nuclei, such as ^{192}Ir .

Nuclear Definitivity and Collective Motion

Ultimately, the shell model reaches limits of tractability when, in heavier nuclei, multiple valence nucleons occupy multiple j shells; and the perturbation matrices, which represent the residual interactions, become very large. Under such circumstances both the number of calculations and limitation on physical interpretation of the results necessitate an alternative

approach [343]. Then it can be advantageous to invoke a collective treatment of the particles in a nucleus. Of general interest to the collective paradigm and to ^{192}Ir in particular is the quantification of non-spherical shape or deformity.

Observations indicate stable, permanent deformation tends to exist in relatively heavy nuclei, whose proton or neutron counts deviate from the magic numbers associated with shell closures. The nuclide regions, shown in Figure 7, where deformity is prevalent are also qualitatively consistent with shell model and state mixing predictions. Indeed, the spherical symmetry of the shell model potential results in spherically symmetric shell states, whose m subspaces are degenerate. However, mixing is possible among states containing unfilled subspaces and non-identical nucleons. Such mixing can lift the degeneracies, leading to non-uniform substate distributions, which are no longer spherically symmetric [34]. This effect may be more pronounced in heavier nuclei, where more valence nucleons populate subspaces far from closure, increasing admixture.

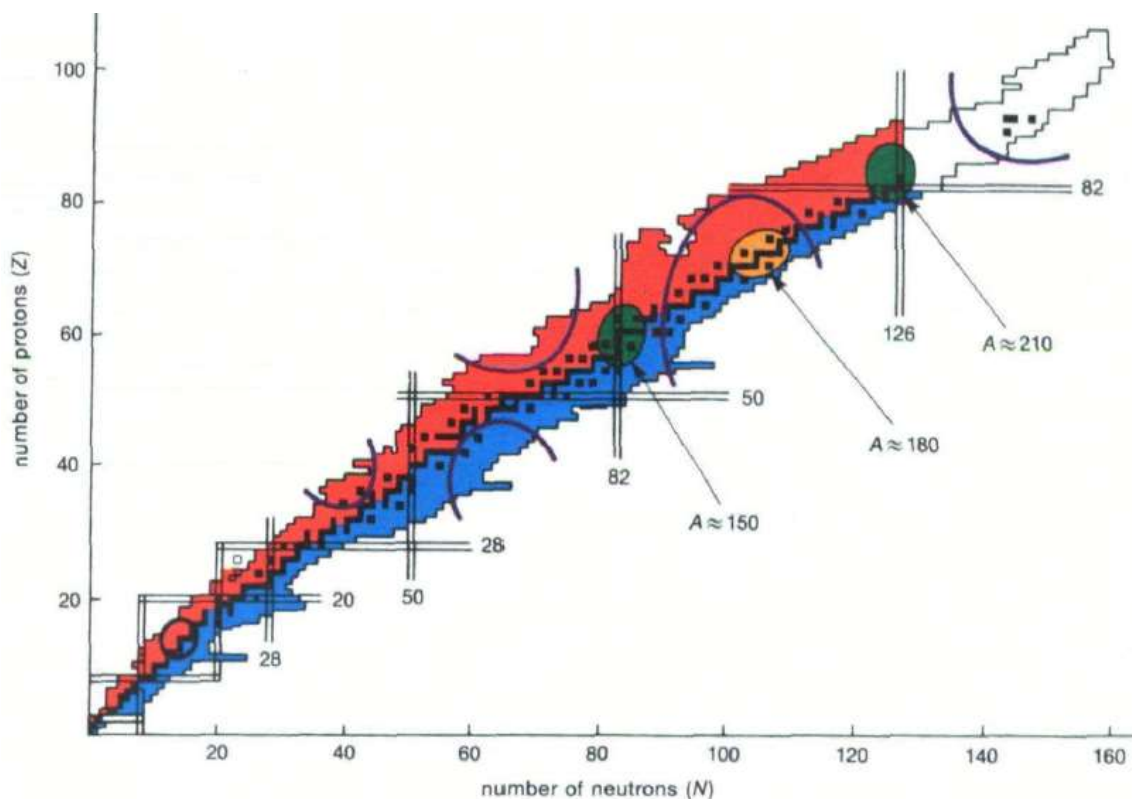


Figure 7. A chart of the known nuclides, with stable nuclides in black. The insides of the purple arcs are regions of deformity and the insides of the colored ellipses are regions where isomerism is common [walker 1994].

It is common to define nuclear shape through a multipole expansion of the radius in the basis of the spherical harmonics. Generally, one may write

$$R(\theta, \phi, t) = R_0 \left(1 + \sum_{\lambda=0}^{\infty} \sum_{\mu=-\lambda}^{\lambda} \alpha_{\lambda\mu}^*(t) Y_{\lambda\mu}(\theta, \phi) \right), \quad (50)$$

for the radius R as a function of the angular coordinates and time, the radius R_0 of a spherical nucleus having equal volume, and time-dependent expansion coefficients α [33]. With respect to their significance in nuclear structure, the important deformation modes of order λ have the following qualitative descriptions [33].

- The $\lambda = 0$ monopole mode has a constant spherical harmonic Y_{00} ; so a non-vanishing expansion coefficient α_{00} implies a change in radius of the sphere. This only occurs dynamically, as the “breathing mode” of the nucleus. However, it is not typically a component of spectra in the energy range, where most models are applicable, due to a high threshold for excitation.
- The $\lambda = 1$ dipole mode corresponds to a translation in the nuclear center of mass and is dismissible as a nuclear deformation or excitation.
- The $\lambda = 2$ quadrupole mode is the most significant for nuclear structure phenomena. It is broadly representative of collective excitations and permanent deformations in most nuclei.
- The $\lambda = 3$ octupole mode corresponds to “pear-shaped” deformations and asymmetric excitations associated with negative parity bands.
- The $\lambda = 4$ hexadecapole mode is the highest mode of significance in nuclear structure theory. It is most frequently used to describe admixtures of quadrupole excitations and the ground state shapes of heavy nuclei.
- Higher-order modes lose physical and practical significance as the node spacing of the spherical harmonics begins to approach the size of an individual nucleon.

In particular, the quadrupole, which is the lowest multipole order describing shape distortion, is typical of many deformed nuclei. Assuming a quadrupole form, it is convenient to relate the expansion coefficients α_{μ} (where $\lambda = 2$ is implicit) in terms of Euler angles such that

$$\alpha_0 = \beta \cos \gamma , \quad (51)$$

$$\alpha_2 = \alpha_{-2} = \beta \sin \gamma . \quad (52)$$

This allows specification of the nuclear shape in terms of β and γ , where β gives the linear extent of the deformation, and γ gives the degree of axial asymmetry. In their ground states, most nuclei are axially symmetric, corresponding to $\gamma = n\pi/3$. With $\beta > 0$ and $\gamma = 0^\circ$, the shape is prolate, corresponding topologically to expansion along one axis of a sphere and compression along the other two. For $\beta > 0$ and $\gamma = -60^\circ$, the shape is oblate, which corresponds to compression along one axis and expansion along the other two. Values of γ not equal to an integer multiple of $\pi/3$ indicate an axially asymmetric or triaxial deformation.

Along the Cartesian axes,

$$\delta R_z = \sqrt{\frac{5}{4\pi}} R_0 \beta \cos \gamma , \quad (53)$$

$$\delta R_x = \sqrt{\frac{5}{4\pi}} R_0 \beta \cos \left(\gamma - \frac{2\pi}{3} \right) , \quad (54)$$

$$\delta R_y = \sqrt{\frac{5}{4\pi}} R_0 \beta \cos \left(\gamma - \frac{4\pi}{3} \right) , \quad (55)$$

give displacements of the nuclear radius, as functions of the deformation parameters; and Figure 8 illustrates the relationship between the Cartesian variables and the deformation parameter γ . Conventionally, one typically takes the z-axis as the symmetry axis.

According to Figure 7, ^{192}Ir appears in the vicinity of a deformation region; and, in fact around the 190 isobar, there exists a shape-transitional region, where nuclei systematically vary between prolate and oblate forms. Data indicate iridium nuclei in the region are typically of axially symmetric prolate character, while nuclei of gold are oblate [3, 5]. Note typical β values in deformed nuclei are around 0.3 [34]. However, observations in the 190 isobar region (and several others) confirm the existence of an exaggerated deformation, with $\beta \sim 0.5$ to 0.6, known

as superdeformation; prolate-oblate shape coexistence in an individual nucleus may also exist in the vicinity of ^{192}Ir [5].

As a result of deformity, a nucleus becomes subject to rotational excitations. However, whereas a classical rotor can rotate about any axis, rotational motion in quantum mechanics is more restrictive. Specifically, a quantum mechanical system with rotational symmetry and no internal structure is rotationally invariant; ergo rotational motion can have no effect on its state. [33] Consequently, rotational excitation about a nuclear symmetry axis is not possible; and an axially symmetric deformed nucleus has two rotational axes perpendicular to the symmetry axis. Additionally, as the broken spherical symmetry in the deformed nucleus lifts the degeneracy of the magnetic m_j substate, new quantum numbers become necessary to specify the state of the system. This will be the subject of more discussion in the deformed shell model.

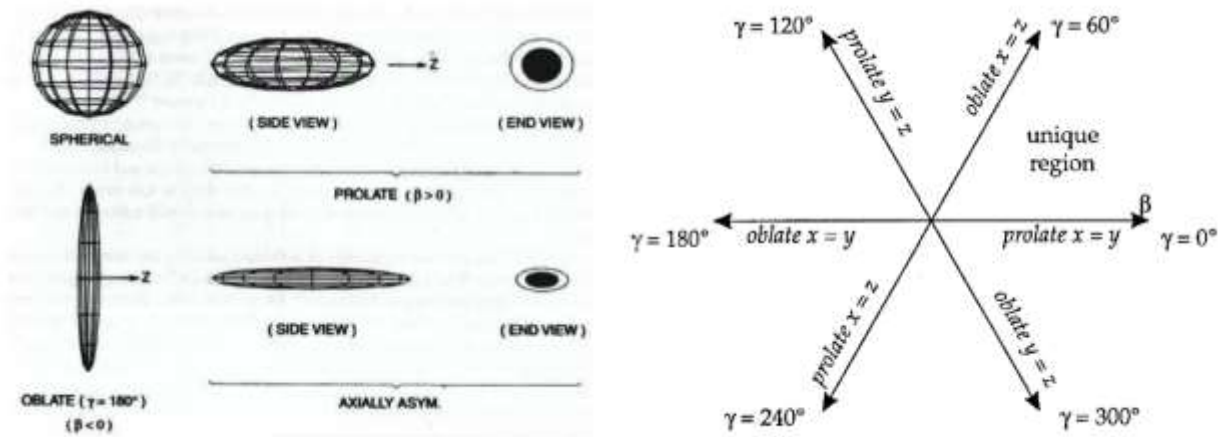


Figure 8. Left: illustration of the equipotential surfaces for various quadrupole-deformed nuclear potentials. Right: graphical depiction of the β - γ plane and the relationship between quadrupole forms with Cartesian axes. By symmetry, the sector from 0° to 60° contains all shapes uniquely. Reproduced from [33, 34].

Important physical properties of a quadrupole deformed nucleus are the moment of inertia,

$$I = \frac{2}{5} AMR_0^2(1 + 0.31\beta), \quad (56)$$

where M is the mass per nucleon, and the electric quadrupole moment,

$$Q_0 = \frac{3}{\sqrt{5\pi}} ZR_0^2\beta(1 + 0.16\beta), \quad (57)$$

where Z is the proton charge. These are given, respectively to first order and second order in β .

Under the assumption collective rotation and intrinsic excitation are separable (adiabatic assumption), one may construct wave functions of the rotational nucleus from the rotational D matrices and the intrinsic wave functions χ_K . Here, K is the angular momentum projection of an intrinsic excitation on the nuclear symmetry axis (z -axis); and, because nuclear rotation can contribute no angular momentum along this axis, K must represent the total projection. Applying wave function symmetry constraints to the degenerate projections K and $-K$, one obtains for the rotational wave function [34]

$$\psi_{JM} = \left(\frac{2J+1}{16\pi^2} \right)^{\frac{1}{2}} (D_{JMK}\chi_K + (-1)^{J-K}D_{JM-K}\chi_{-K}). \quad (58)$$

For axially symmetric nuclei, having rotation of equal frequencies about the non-symmetry (x and y) axes, the rotational Hamiltonian is

$$H = \frac{\hbar^2}{2I} \mathbf{R}^2, \quad (59)$$

with rotational angular momentum operator \mathbf{R} . Initially taking $K = 0$, (58) allows only even values of J [42], and also assuming a 0^+ ground state (an acceptable assumption for an even-even nucleus), (59) returns the energy of a symmetric top,

$$E_{rot}(J) = \frac{\hbar^2}{2I} J(J+1). \quad (60)$$

The allowed integer values of $J > 0$ thus form a rotational band – a common feature in the spectra of deformed nuclei. The ratio

$$\frac{E(J=4)}{E(J=2)} = \frac{E_{4_1^+}}{E_{2_1^+}}, \quad (61)$$

nearly constant at 3.33 in the deformed region, constitutes a well-known signature of deformation and rotational motion [34]. Note also, the lowest energy states for a given angular

momentum are known as yrast states (yrast being the superlative of the Swedish adjective for dizzy); and they broadly follow the $J(J+1)$ trend.

When K is not equal to zero, (58) subject to (59) gives, relative to the energy of the intrinsic excitation, the rotational energy

$$E_{rot}(J) = \frac{\hbar^2}{2I} (J(J+1) - K(K+1)), \quad (62)$$

where J can take the value $K + n$ for any integer n . Thus, in a single nucleus, there may exist multiple rotational bands, with each “built” on “band-heads” of unique intrinsic excitations and associated K (z -axis) projections. However, observations show the moment of inertia (and hence the deformation) generally is not a constant among the various bands [34]. It is then conceivable



Two bands, with band-heads at different energies, may approach one another if the lower energy band-head is associated with a lower moment of inertia. While the bands cannot truly cross, they may mix and exchange structure as they converge in a phenomenon known as “band-crossing” [34]. If the low band-head, perhaps the true nuclear ground state, initially represents yrast, the wave functions of the yrast states will, after the crossing, assume the character of the higher band-head.

In addition to rotation, vibrational degrees of freedom also exist in deformed nuclei. Not surprisingly, when the nucleus is quadrupole deformed, the vibrational modes tend to be of quadrupole character, carrying two units of angular momentum. Such modes fall into two categories: the axially symmetric β vibrations having $K = 0$, and the axially asymmetric γ vibrations having $K = 2$. Qualitatively, the β mode involves compression and expansion along the z axis. This corresponds to an oscillation in the β component of the deformation; and thus preserves axial symmetry. The γ mode involves oscillations in the γ component of deformation. These are perpendicular to the z -axis resulting in time-dependent excursions from axial symmetry. As a consequence of the momentary asymmetry, the nucleus is able to rotate around the z -axis and contribute a $K = 2$ angular momentum projection in the z -direction. Quadrupole vibrational motion is significant in that it can couple to the rotation and mix the rotational bands; it is also common among low-lying states of odd-odd rare earths [5].

The Deformed Shell (Nilsson) Model

The deformed shell model, often called the Nilsson model, extends the basic concepts of the spherical shell model to describe single-particle states in a deformed potential. Conceptually, one may begin by substituting a three-dimensional harmonic oscillator

$$\frac{1}{2}m\omega_0'^2 R^2 = \frac{m}{2}(\omega_x^2 x^2 + \omega_y^2 y^2 + \omega_z^2 z^2), \quad (63)$$

for the one-dimensional system in the spherical case, where $\hbar\omega_0'$ is the oscillator constant of the equivalent spherical nucleus [33]. This defines a nuclear potential surface of ellipsoidal geometry with distinct oscillator constants in the different spatial directions. The full Hamiltonian then becomes [42]

$$H = -\frac{\hbar}{2m}\nabla^2 + \frac{m}{2}(\omega_x^2(x^2 + y^2) + \omega_z^2 z^2) - Cl \cdot s - D(l^2 - \langle l^2 \rangle_N), \quad (64)$$

under the constraint of axial symmetry

$$\omega_x = \omega_y. \quad (65)$$

Note the presence of the spin-orbit and l^2 terms. As in the spherical model, the l^2 term serves to correct for the steep rise in the harmonic oscillator potential at the nuclear surface [33]. Subtraction of the

$$\langle l^2 \rangle_N = N(N + 3)/2 \quad (66)$$

term is intended to ensure proper spacing of the shells below $\hbar\omega_0'$ [42].

Given the additional constraint of volume conservation,

$$\omega_0'^3 = \omega_x \omega_y \omega_z, \quad (67)$$

a second order expansion of ω_0' in the small parameter δ yields

$$\omega_0 = \left(1 + \frac{2}{9}\delta^2\right)\omega'_0. \quad (68)$$

This is indicative of a quadrupole deformation; and in terms of the spherical harmonic Y_{20} the potential becomes

$$V(r) = \frac{1}{2}m\omega_0^2\mathbf{r}^2 - \beta_0m\omega_0^2\mathbf{r}^2Y_{20}(\theta, \phi) \quad (69)$$

with

$$\beta_0 = \frac{4}{3}\sqrt{\frac{4\pi}{5}}\delta. \quad (70)$$

It is worthwhile to mention the deformation, here an expansion of the potential, is distinct from the radial expansion applied in the collective description of the nucleus. [33] shows they are related by the spherical harmonic expansion coefficient $\lambda\mu = 20$ according to

$$\left[\frac{R_z}{R_x}\right]_{collective} = \left[\frac{R_z}{R_x}\right]_{Nilsson} \approx 1 + \frac{3}{2}\alpha_{20}\sqrt{\frac{5}{4\pi}}; \quad (71)$$

And therefore one may take the collective β defined in (51) and (52) equal to β_0 in (70), giving $\delta \approx 0.95\beta$ [34].

It is now possible, in the limit of small deformation ($\beta < 0.4$), to define the Nilsson model Hamiltonian [33]

$$H = -\frac{\hbar}{2m}\nabla^2 + m\omega_0^2\mathbf{r}^2\left(\frac{1}{2} - \beta_0Y_{20}(\theta, \phi)\right) - \hbar\omega'_0\kappa(2\mathbf{l} \cdot \mathbf{s} + \mu\mathbf{l}^2), \quad (72)$$

with $\kappa = C/2\hbar\omega_0$ and $\mu = 2D/C$. The variables κ and μ are free parameters, which fit to data. They may be different for protons and neutrons but typically have respective values on the order of 0.05 and 0.3 [33].

A phenomenological discussion of the Nilsson model begins with a single valence nucleon

occupying a j orbit in the deformed potential. Clearly, due to the deformity, the m_j magnetic substates can no longer be degenerate because the distribution of the potential results in different magnitudes of attraction for different orbital orientations. When considering a prolate, quadrupole-deformed potential, an orbit in the equatorial plane, containing the symmetry axis, experiences a greater attraction than a polar orbit of the same j . Consequently, the equatorial orbit exists at a lower energy than its polar counterpart. Generally speaking then, the energy of a single nucleon orbit is related to its projection onto the symmetry axis, as depicted in Figure 9, with lower projections indicating more tightly bound orbits. Conventionally, one uses the label Ω for a single particle projection, and K for the total projection. However, because the collective nuclear spin can have no component along the symmetry axis, K reduces to the sum of the individual particle projections. Therefore, in the case of a single, particle $K = \Omega$.

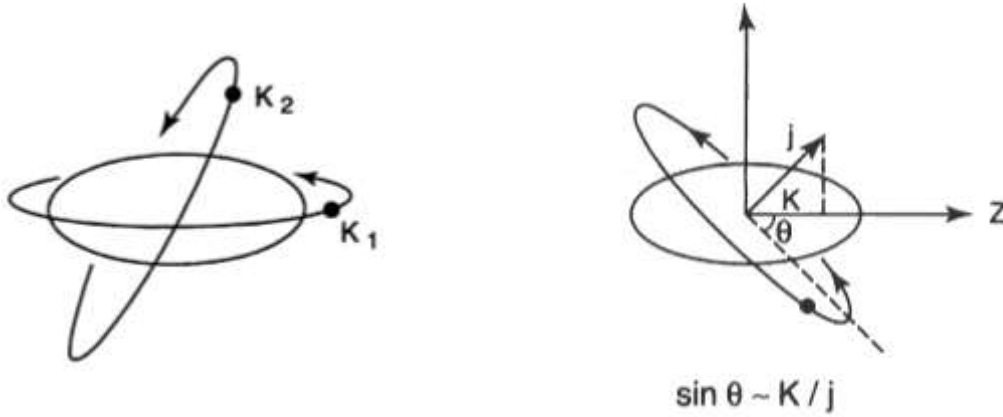


Figure 9. Notional drawings of a single-particle orbit³ and angular momentum projections in a deformed potential. Reproduced from [34].

Upon considering, with respect to the ratio $x = K/j$, the derivative of the approximate classical orbit angle

$$\frac{d}{dx}(\theta = \arcsin(x)), \quad (73)$$

it is evident the energy spacing of adjacent K varies with x . The spacing is small for x near zero, becoming infinite as x approaches unity; and it exhibits approximately linear variation with the magnitude of deformation. Such “ K -splitting” illustrated in Figure 10 is one of two principal phenomenological features of the Nilsson model. The other is the admixture of initially distinct K states, which can approach one another in energy as the nuclear deformation changes.

The quadrupole deformation of the potential ensures the strongest mixing is quadrupole in nature. This favors mixing matrix elements, whose configurations share the same spin orientation, K , and parity but differ by two units of angular momentum [34]. However, the energy spacing of the configurations is also a factor; and closely spaced configurations can mix even if their configurations do not favor quadrupole interaction. As with the rotational bands, the configurations may converge to an inflection point and exchange principal wave function components; but they never cross. It is also worth noting: (1) the effects considered tend to increase in strength as the shells get higher; and (2) the wave functions for the highest K values in a given shell tend to be pure. Point (1) is, with respect to deformation, a consequence of greater energy change for nucleons orbiting at larger radius. Point (2) arises because the high- K configurations, which the spin-orbit interaction depresses from higher shells, have “unique parity”, incompatible with the surrounding configurations [34].

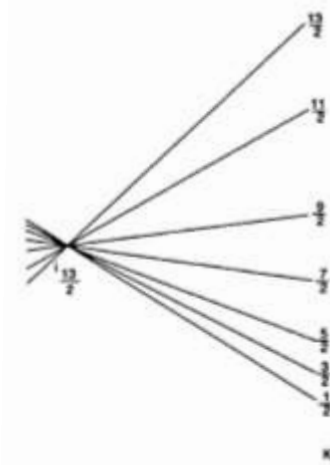


Figure 10. Illustration of K -splitting or the energy separation of K orbitals as a function of nuclear deformation. Reproduced from [34]

The Nilsson diagram in Figure 11 nicely illustrates the phenomenological features of the model. Configuration labels in the illustration follow the conventional format

$$K^{\pi}[Nn_z\Lambda], \quad (74)$$

where K^{π} is the K -projection and parity, N is the quantum number of the principal oscillator shell, n_z is the number of wave function nodes in the z -direction, and Λ is the projection of the orbital angular momentum on the z -axis. Label elements are subject to the following constraints.

- $K = \Lambda + \Sigma = \Lambda \pm 1/2$, where Σ represents the projection of the intrinsic spin on the z -axis.
- $K \geq 1/2$, with $1/2$ representing the lowest possible projection of angular momentum onto the z -axis, or equivalently the most tightly bound equatorial orbit.
- $n_z \leq N$.
- The sum of n_z and Λ must be even if N is even and odd if N is odd.

The Nilsson wave functions are linear combinations of the spherical shell model wave functions according to

$$\psi_{Nils} = \sum_j C_j^i \phi_j, \quad (75)$$

where the C are configuration mixing coefficients. Crude estimates of the mixing coefficients are possible using the diagram by considering the relative position of a configuration between two parent spherical states and inflection points at lesser values of deformation [34].

Returning now to the Hamiltonian (72) it is evident the set of terms, other than the term in Y_{20} , effectively represents the spherical shell model Hamiltonian. Thus one may treat the Y_{20} term as a perturbation and evaluate it in the basis of the spherical wave functions, giving relative to the spherical potential, the shift in energy

$$\Delta E(NljK) = -\frac{2}{3}\hbar\omega_0 \left(N + \frac{3}{2} \right) \delta \frac{(3K^2 - j(j+1)) \left(\frac{3}{4} - j(j+1) \right)}{(2j-1)j(j+1)(2j+3)}, \quad (76)$$

[34]. The following observations are now worth noting [34]:

- The energy shift expression explains the preponderance of downward sloping orbits in the Nilsson diagram. It is possible to deduce ΔE is negative for $K/j > 0.65$, which corresponds to orbital inclinations greater than 40° .
- The slope of the energy shifts must be steeper for larger N , all else equal. This implies

larger nuclei are easier to deform.

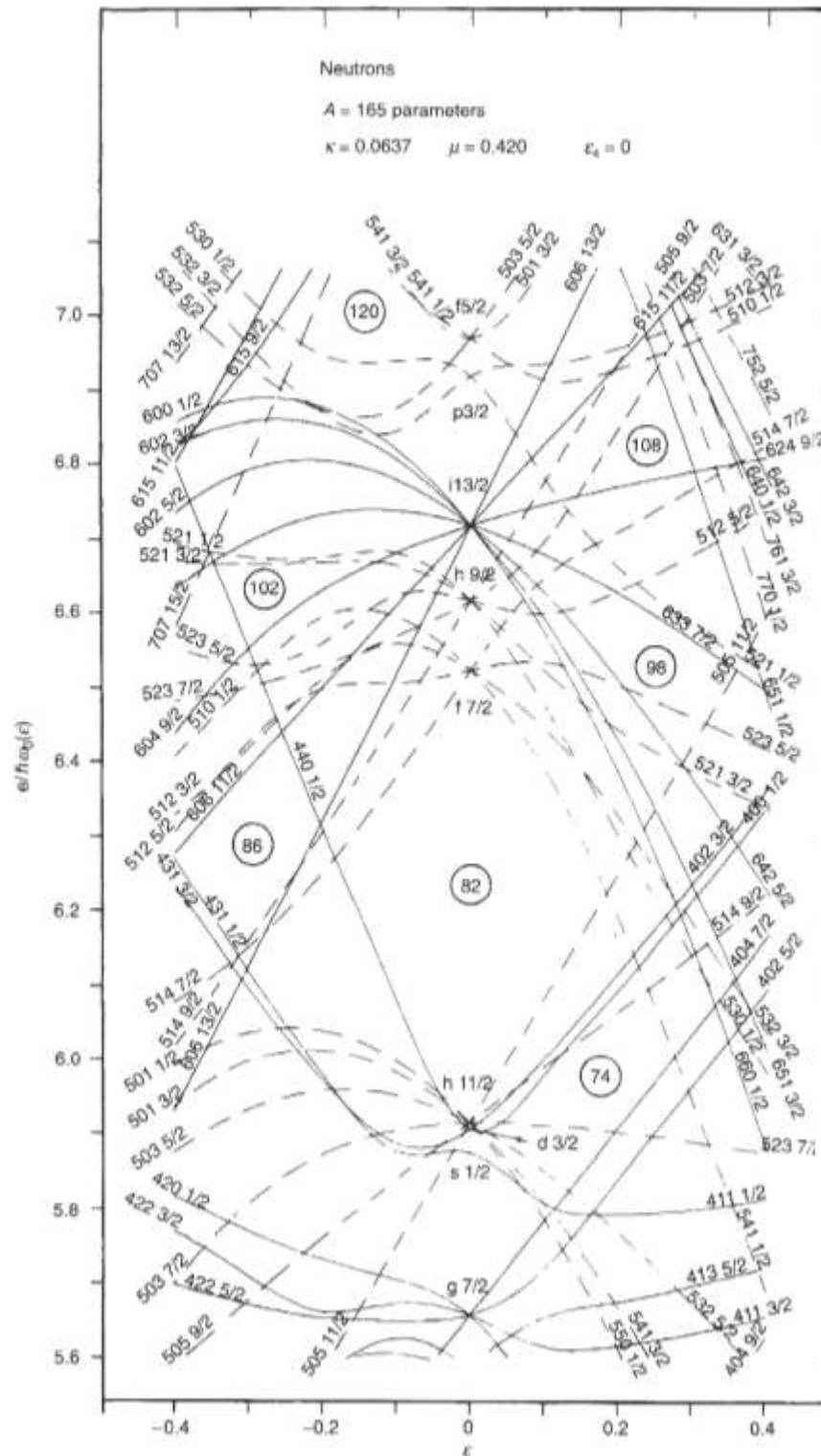


Figure 11. Nilsson Diagram for single neutron orbitals in the $150 < A < 190$ region as a function of the deformation parameter $\varepsilon \approx 0.95\beta$. Solid and dashed lines respectively represent orbitals with positive and negative parity.

Reproduced from [42].

In the limit of large deformation*, the l^2 and spin-orbit terms become trivial; then the Nilsson Hamiltonian takes the form of an anisotropic harmonic oscillator with eigenvalues

$$E(n_x, n_y, n_z) = \hbar\omega_x(N - n_z + 1) + \hbar\omega_z\left(n_z + \frac{1}{2}\right), \quad (77)$$

corresponding to independent motions along the z -axis and in the xy -plane. Reflecting the energetic preference for equatorial orbits, the energies asymptotically lose their dependence on Λ , in favor of pure dependence on n_z [34]. This asymptotic behavior is illustrated in Figure 12.

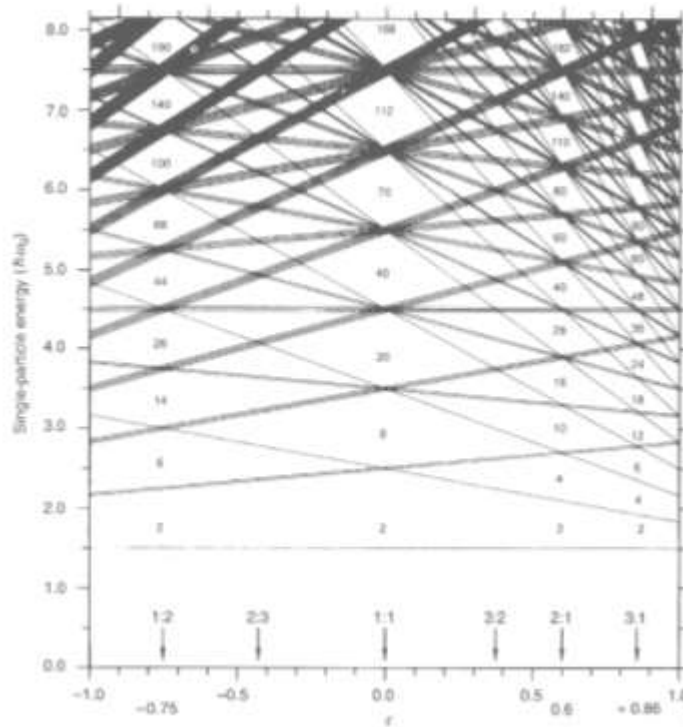


Figure 12. Asymptotic single particle energies of the axially symmetric harmonic oscillator. The integer ratios give the frequency of vibration in the x - y plane to the frequency in the z -direction and correspond to values of ε where degeneracy is high. Reproduced from [42].

The Particle-Plus-Rotor Model

* A more rigorous mathematical treatment in [42] divides deformity into three regions, among which the limit for small β is taken to be ~ 0.1 ; and a full diagonalization of the mixing matrix is carried out in the intermediate region.

To further generalize the description of nuclear structure phenomena, it is advantageous to develop models, which combine the single-particle and collective paradigms. The particle-plus-rotor model is one such example, frequently applied to odd-A, deformed nuclei. In this case, the total nuclear spin \mathbf{J} is the sum of (1) the single-particle spin \mathbf{j} , which originates from the motion of the odd particle in a deformed potential, and (2) the collective spin \mathbf{R} , which originates from an even-even core of paired nucleons.

Building on (59), the rotational Hamiltonian now takes the form

$$H_{rot} = \frac{\mathbf{R}^2}{2I} = \frac{\hbar^2}{2I} \left((J_x - j_x)^2 + (J_y - j_y)^2 \right) \quad (78)$$

$$= \frac{\hbar^2}{2I} \left(J^2 - J_z^2 + [j_x^2 + j_y^2] + [-(J_+ j_- + J_- j_+)] \right) \quad (79)$$

where

$$J_{\pm} = J_1 \pm iJ_2, \quad (80)$$

$$j_{\pm} = j_1 \pm ij_2. \quad (81)$$

More succinctly,

$$H_{rot} = \frac{\hbar^2}{2I} \left(J^2 - J_z^2 + [H_{recoil}] + [H_{rpc}] \right). \quad (82)$$

According to a classical interpretation, the rotation-particle coupling term H_{rpc} arises from the centrifugal and Coriolis forces, which couple the motion of the valence particle in the deformed potential to the motion of the core [42]. Treatment of this coupling typically falls into one of the two limiting cases, which Figure 13 illustrates.

When both J and j are small, the Coriolis component in the rotational Hamiltonian is weak and the collective nuclear rotation has trivial influence on intrinsic structure. Upon making these assumptions, the adiabatic approximation, allowing separation of the single-particle and collective degrees of freedom, is applicable. Consequently, $\Omega = K$ remains a good quantum number and j precesses about the symmetry axis. This is the deformation-aligned or strong

coupling scheme, depicted on the left in Figure 13. When the Coriolis interaction becomes significant, the adiabatic approximation is no longer valid; and independent treatment of collective and intrinsic behavior is not possible. Under these circumstances, alignment of the single-particle and rotational motion is energetically favorable. Consequently, j precesses about the rotation axis and K changes dynamically, ceasing to be a useful representation of the system. This is the rotation-aligned or weak coupling scheme, depicted to the right in Figure 13.

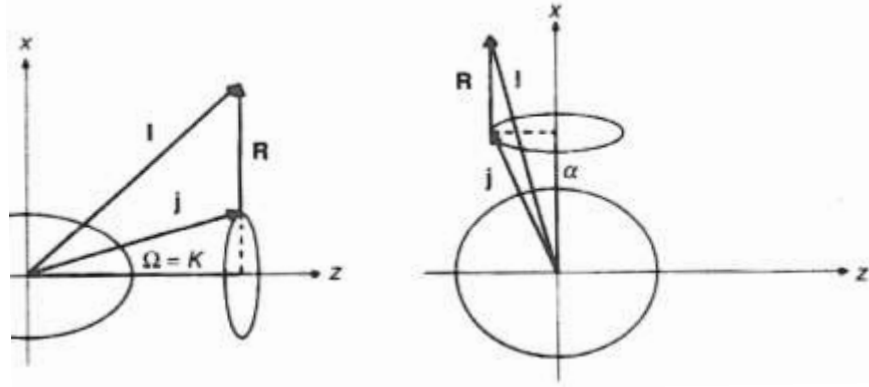


Figure 13. Illustration of the two coupling extremes. The figure on the left represents deformation alignment, with j precessing about the symmetry axis and K nearly constant. The figure on the right depicts rotation alignment, with j now precessing about the rotation axis and K no longer constant. Reproduced from [42, 43]

In the strong coupling scheme, one may assume the coupling term is small, such that only its diagonal elements in the mixing matrix are significant; and it may be treated through first-order perturbation theory. Moreover, the selection rules for $j_{\pm/}$ are $\Delta\Omega = \pm 1$, and each odd-particle orbit has two-fold degeneracy, corresponding to a difference in sign. Therefore, diagonal coupling terms are non-vanishing only for $\Omega = \pm 1/2$.

Given rotational bands are built on single-particle states, it is evident the recoil term depends only on the intrinsic particle wave functions and is constant with respect to R . This term is also small and may be neglected to first order [42]. Thus, upon including (64), the single-particle Hamiltonian H_{sp} , the full Hamiltonian is

$$H = H_{sp} + H_{rot} . \quad (83)$$

Wave functions are constructed in a body-fixed coordinate system from the rotational D matrices with the intrinsic and conjugate single-particle wave functions projected in an $|Nlj\Omega\rangle$ -basis,

$$\varphi_i = \sum_{Nj} a_{Nlj\Omega}^i |Nlj\Omega\rangle, \quad (84)$$

$$\varphi_i^\sim = \sum_{Nj} (-1)^{j-\Omega} a_{Nlj\Omega}^i |Nlj-\Omega\rangle. \quad (85)$$

Under the constraint of invariance with respect to 180° rotation about the x -axis (R1 symmetry), these wave functions are

$$\psi_{J\Omega M} \propto (D_{JM\Omega} \chi_K + (-1)^{J-\Omega} D_{JM-\Omega} \chi_{-\Omega}), \quad (86)$$

equivalent, within a proportionality factor, to (58). The eigenvalues of this system are the energies of the rotational bands

$$E_{IK} = |\varepsilon_i - \lambda| + \frac{\hbar^2}{2I} \left(J(J+1) - \Omega^2 + \delta_{\Omega\frac{1}{2}} a (-1)^{J+\frac{1}{2}} \left(J + \frac{1}{2} \right) \right), \quad (87)$$

in the strong coupling approximation [42]. As in the quasiparticle energy (47), the ε_i are the eigenvalues of the single-particle Hamiltonian; and the single-particle energies are thus taken with respect to the Fermi surface. Should one include the effects of the pairing interaction, the quasiparticle energy replaces the single-particle expression. The quantity a is termed the decoupling parameter, which is calculated according to

$$\langle \varphi_i | j_\pm | \varphi_i^\sim \rangle = \sum_{Nj} (-1)^{j-\frac{1}{2}} \left(j + \frac{1}{2} \right) \left| a_{Nlj\frac{1}{2}}^i \right|^2. \quad (88)$$

In a $K = \frac{1}{2}$ band, specific pairs of states $\{(1/2, 3/2), (5/2, 7/2), \dots\}$, separated by $\Delta K = 1$, may become degenerate as a result of the decoupling.

In general, Coriolis and centrifugal forces do not amount to a small perturbation as in the strong coupling, deformation-aligned scheme. This is evident upon rewriting the particle-rotor Hamiltonian to give

$$H = H_{sp} + \frac{\hbar^2}{2I} (\mathbf{J}^2 + \mathbf{j}^2 - 2\mathbf{J} \cdot \mathbf{j}). \quad (89)$$

Here, the principle of energy minimization dictates the alignment of \mathbf{J} and \mathbf{j} becomes energetically favorable when either or both are large [42]. Additionally, as \mathbf{R} , the collective rotational component of \mathbf{J} , can have no projection along the symmetry axis, the effect of the alignment is to orient \mathbf{j} parallel to the rotation. When this is the case, as the right-hand drawing in Figure 13 suggests, it becomes convenient to redefine the intrinsic states according to their projections α along the rotation axis. Thus

$$\varphi_\alpha = \sum_{\Omega} C_{\Omega} \varphi_{\Omega}, \quad (90)$$

[42] where the transformation coefficients are given by

$$D_{\alpha\Omega}^j \left(0, \frac{\pi}{2}, 0 \right). \quad (91)$$

One can then compute the energies in the rotation-aligned scheme according to

$$E = \sum_{\Omega} 2|C_{\Omega}|^2 (\varepsilon_{\Omega} - \lambda) + \frac{\hbar^2}{2I} (J(J+1) + j(j+1) - 2J\alpha), \quad (92)$$

where again the first term represents the single particle contribution to the energy relative to the Fermi surface. Note the contribution of this term is directly related to the orbital energy spacing ($\Delta\Omega = 1$), which in turn depends directly on the deformation. Consequently, the eigenstate energies of the rotation-aligned system can grow as deformation increases; and thus, larger deformations can become less favorable to rotational alignment [42]. The systematics of this phenomenon are illustrated in Figure 14, where different orbital energies are plotted for both coupling schemes, as functions of deformation. Due to the R1 symmetry of the rotation aligned nucleus, even- J states are also energetically favored over odd- J states.

In the extreme case the rotation is fully aligned, a simplification of (92) results from the fact that $\alpha = j$, whereby

$$E_{rot} = \frac{\hbar^2}{2I} (J(J+1) + j(j+1) - 2J\alpha) \quad (93)$$

$$= \frac{\hbar^2}{2I} (J - \alpha)(J - \alpha + 1) + 2\alpha \quad (94)$$

$$= \frac{\hbar^2}{2I} R(R + 1) + \text{constant} , \quad (95)$$

with $R = J - \alpha$. Clearly, to within the constant offset, this is equivalent to the expression (60) for a symmetric top, which determines the energy spacing in rotational bands of even-even nuclei [42]. Rotational bands in rotation-aligned spectra of an odd-A nucleus should then have spacing nearly identical to those of its even-even neighbors.

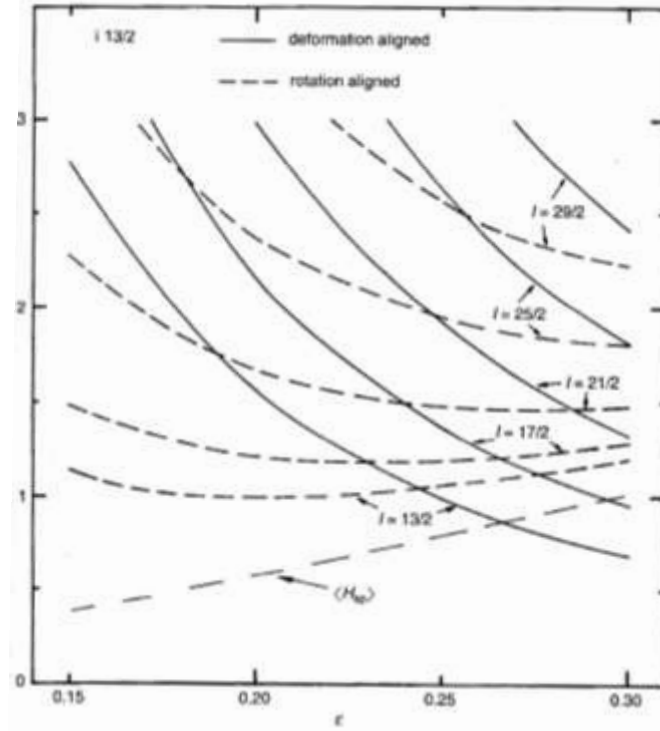


Figure 14. Notional illustration comparing eigenstate energies for deformation aligned and rotation aligned coupling. It is evident in the figure larger deformation and lower spin favor deformation alignment. Reproduced from [42].

Modeling Prolate-Deformed, Odd-Odd Nuclei

Of particular concern to the study of the ^{192}Ir nucleus are its aspherical shape and the doubly odd nature of its nucleon counts. Both attributes result in broken symmetries, which give rise to individual particle and collective degrees of freedom. These attributes significantly complicate ^{192}Ir theoretical description and empirical observation [3, 5]. Presently, the most common theoretical interpretation of observed ^{192}Ir spectra involves application of the two-quasiparticle-

plus-axially-symmetric-rotor model (TQPRM) to the identification of rotational bands, built on Nilsson configurations [5].

Thus far the discussion focused on models particular only to even-even or odd-A nuclei. Due to empirical and theoretical complexity, and perhaps because of disagreement on a proper theoretical description, odd-odd, deformed nuclei are rarely mentioned in most texts. However, there is a reasonable body of research on this topic. In 1998, A Jain et al. published a survey of the available literature and the contemporary prescription for developing a practical TQPRM description of doubly-odd, prolate-deformed nuclei. Based on the most recent publications [3, 8], it appears their approach remains valid.

The TQPRM is detailed in [44, 45]; its construction begins with a Hamiltonian of the form (83), where the single-particle term is now called the intrinsic Hamiltonian H_{intr} . In addition to the mean field potential H_{av} , which again is the Nilsson model Hamiltonian (64), H_{intr} incorporates a short-range residual interaction V_{pn} , between the odd proton and odd neutron, such that

$$H_{intr} = H_{av} + V_{pn} . \quad (96)$$

In general, H_{intr} also includes a vibrational component and a pairing interaction between the odd nucleons; but one can ignore these terms to good approximation [5].

The rotational component H_{rot} of the full TQPRM Hamiltonian is (82), modified on account of single-particle contributions from two particles. This results in the additional particle-particle coupling term H_{ppc}

$$H_{ppc} = \frac{\hbar^2}{2I} (\mathbf{j}_{p+} \mathbf{j}_{n-} + \mathbf{j}_{p-} \mathbf{j}_{n+}) , \quad (97)$$

with the operators $j_{p\pm}$, $j_{n\pm}$ defined according to (80) and (81). There also results a modification to the recoil term, giving

$$H_{recoil} = \frac{\hbar^2}{2I} ([j_x^2 + j_y^2]_p + [j_x^2 + j_y^2]_n) , \quad (98)$$

where subscripts on the square brackets denote respective contributions of the proton and neutron. Note the primary contributions of the recoil term are diagonal in the mixing matrix and off-diagonal terms need not be considered [5]. The rotational Hamiltonian is now

$$H_{rot} = H_R + H_{recoil} + H_{ppc} + H_{rpc} \quad (99)$$

Where H_R , is the collective rotational Hamiltonian (59); and the complete TQPRM Hamiltonian is

$$H = H_{intr} + H_{rot} = H_{av} + V_{pn} + H_R + H_{recoil} + H_{ppc} + H_{rpc} . \quad (100)$$

Under the assumption of an axially symmetric, quadrupole deformation, one takes the single particle states of the odd proton and odd neutron to be the asymptotic Nilsson quantum numbers (74). As an approximation for the effects of pairing on the single particle energies, it is convenient to replace the single-particle energies of the odd nucleons with the respective quasiparticle energies. Taking ε_0 to lie on the Fermi surface, the quasiparticle energies become

$$E_{qp} = \sqrt{(\varepsilon_i - \lambda)^2 + \Delta^2} + \Delta , \quad (101)$$

where Δ usually assumes the value of the empirical pairing gap parameter between neighboring even-even and odd-A nuclei. One also typically assumes the quasiparticle energies include the diagonal mixing matrix contributions of the recoil interaction; and thus, the recoil term may be discarded entirely [5].

In the deformation-aligned, strong-coupling scheme, the Nilsson configuration of an odd-odd nucleus is determined through the additive combination of the single-quasiparticle energies and angular momentum projection quantum numbers. The linear combination of the single-particle angular momenta then results in a pair of degenerate band heads at

$$K_{><} = |\Omega_p \pm \Omega_n| , \quad (102)$$

for each two-quasiparticle configuration. On the Nilsson configuration band heads of the various two-quasiparticle excitations, rotational excitations build at integer spacing $J = K + n$, according to (62); and the unperturbed energy levels become

$$E_{JK} = [E_{qp}]_p + [E_{qp}]_n + \frac{\hbar^2}{2I} (J(J+1) - K^2). \quad (103)$$

For the unperturbed Hamiltonian $H_{av} + H_R$, and two-quasiparticle configurations $\alpha_\rho = \rho_p \rho_n$, wave functions take the form of (86) according to

$$\begin{aligned} |IMK_{\alpha_\rho}\rangle = & \left(\frac{2J+1}{16\pi^2(1+\delta_{K0})} \right)^{1/2} \left(D_{MK}^J |K_{\alpha_\rho}\rangle \right. \\ & \left. + (-1)^{J+K} D_{M-K}^J R_i |K_{\alpha_\rho}\rangle \right), \end{aligned} \quad (104)$$

where R_i is the rotation operator

$$e^{-i\pi a}, \quad (105)$$

with signature quantum number $\alpha = 0, 1$ and eigenvalues

$$r = e^{-i\pi j_1}. \quad (106)$$

Thus far, the model accounts for the mean field, collective rotation, and the recoil terms in the TQPRM Hamiltonian. However, two sets of empirical observations invite adjustments, which partially account for the remaining terms. These are Gallagher-Moszkowski (GM) splitting [46] and the Newby shift (N-shift) [47]. Phenomenologically, the p-n interaction V_{pn} , and to some extent the zero-point rotational energy, lift the two-fold degeneracy of the quasiparticle band-heads (102). Relative placement of the two resulting band heads (known as a GM doublet) is determined by the empirical GM rule, which says the spin-parallel triplet (K_t) band head lies lower in energy than the spin-antiparallel (K_s) band head. When corrected for the zero-point rotational energy, the difference between K_t and K_s defines the GM splitting. As an additional consequence of the p-n interaction and the special symmetry of a $K = 0$ wave functions, odd and even levels (odd and even J) of $K = 0$ bands experience displacement relative to one another, resulting in the N-shift. Determination of the GM splitting in such bands is therefore dependent upon an N-shift correction.

Specifically, under the rotation operation R_i , the $K = 0$ wave function

$$|K = 0, \alpha_\rho\rangle = \frac{1}{\sqrt{2}}(|\rho_p\Omega\rangle|\rho_n - \Omega\rangle - r|\rho_p - \Omega\rangle|\rho_n\Omega\rangle), \quad (107)$$

is non-vanishing for odd values of J , when the eigenvalue r is one; and it is non-vanishing for even values of J , when the r is zero. These two branches are modified differently by the diagonal terms of V_{pn} resulting in the odd-even energy shift, given as

$$S = (-1)^J \langle \rho_p\Omega; \rho_n - \Omega | V_{pn} | \rho_p - \Omega; \rho_n\Omega \rangle = (-1)^J B_N. \quad (108)$$

Thus one may assimilate these adjustments, into (103) and obtain, for energy states of an odd-odd nucleus, the expression

$$\begin{aligned} E_{JK} = [E_{qp}]_p + [E_{qp}]_n + \frac{\hbar^2}{2I} (J(J+1) - K^2) + [E_k]_{int} \\ + (-1)^J \delta_{K,0} ([E_{K=0}]_{int} + E_a). \end{aligned} \quad (109)$$

The terms with the “int” subscript represent the diagonal contributions of the residual p-n interaction. Analogous to (87), the term E_a is the diagonal rotation-particle coupling contribution, which is non-vanishing only for $\Omega_p = \Omega_n = 1/2$ and subject to the decoupling parameters, such that

$$E_a = -\frac{\hbar^2}{2I} a_p a_n \delta_{\Omega_p, 1/2} \delta_{\Omega_n, 1/2} \delta_{K,0}. \quad (110)$$

The GM splitting and N-shift are then respectively defined according to the relations

$$\Delta E_{GM} = [E_{k<}]_{int} - [E_{k>}]_{int} \quad (111)$$

$$B_N = [E_{k=0}]_{int} \quad (112)$$

At this point it is important to reemphasize these corrections consider only diagonal contributions from the p-n interaction and Coriolis terms in the Hamiltonian. To go any further requires, for the p-n interaction, construction of a parameterized phenomenological form, to which one can fit empirical observations of the N-shifts and GM splitting. While Jain et al. detail this procedure using a form of the p-n interaction described in Boisson et. al [48], they concede

consensus on that choice is unclear; and acknowledge, for instance, others were able to obtain spectra with a delta interaction [49].

P. Prokofjevs et al. [50] applied with reasonable success, the prescription, described thusly, to ^{166}Ho , which is one of the best known odd-odd nuclides [5]. However, a couple of unusual considerations may complicate such application to ^{192}Ir . These are, specifically, a possible violation of the GM rule, in the form of a missing $K^\pi = 6^-$ band head, and possible coexistence of prolate and oblate shapes.

Nuclear Transitions

A nucleus in an excited state decays to the ground state through electromagnetic transitions in the form gamma radiation and internal conversion (emission) of atomic shell electrons. These transitions involve changes in both energy and angular momentum; and are governed by a field, which one usually represents through a multipole expansion in the spherical harmonics.

Quantum Mechanical Treatment

Generally, one treats transitions in a quantum mechanical system using time-dependent perturbation theory according to the equation

$$i\hbar \frac{d\psi}{dt} = (H_0 + \lambda H')\psi_n, \quad (113)$$

with H_0 and H' defined as they were in (17). When the transition occurs between two states ψ_i and ψ_f , which lie in a band of energies, as is the case in a nucleus, the general result for the transition rate (or decay constant) λ is Fermi's Golden Rule [35, 40]

$$\lambda = \frac{2\pi}{\hbar} |V'_{fi}|^2 \rho(E_f). \quad (114)$$

Here, $\rho(E_f)$ is the density of final states, and V'_{fi} is the transition matrix element, given, as it was in (23), by

$$V'_{fi} = \langle \psi_f | V' | \psi_i \rangle, \quad (115)$$

where the subscripts i and f represent the initial and final states, respectively.

Lifetimes

The time-dependence of (113) implies the system is not a stationary state; and its solution with eigenvalue E_n is [35]

$$\psi_n(r, t) = \psi_n(r) e^{-iE_n t/\hbar} e^{-t/2\tau_n}. \quad (116)$$

Consequently, the probability of finding the system in the initial state decays exponentially with time, as one would expect in a nuclear transition process. According to the Heisenberg uncertainty principle, this finite lifetime dictates uncertainty must exist in the energy E_n . One may precisely quantify the uncertainty as the Fourier transform of the decaying exponential, which gives

$$P(E)dE = \frac{dE}{(E - E_n)^2 + \Gamma_n^2/4}, \quad (117)$$

where the uncertainty relation determines the energy width of the state as

$$\Gamma_n = \frac{\hbar}{\tau_n}. \quad (118)$$

The resulting distribution (117) represents the probability $P(E)dE$ for observing the system in the energy range $E + dE$. In the case where the energy spacing between adjacent states is much less than the width of either state, the states become indistinct and transition radiation exists as a spectral continuum. Under such conditions, a multiplicity of overlapping, available states, which can participate in a transition, determine the density of states in (114). Low-level nuclear states, with lifetimes on the order of picoseconds [35], very often represent the opposite extreme; and their widths have trivial effect on the discrete nature of the transitions.

The quantum mechanical description of state lifetimes is also the basis of the familiar radioactive decay law,

$$N(t) = N_0 e^{-\lambda t}, \quad (119)$$

which represents the number of systems $N(t)$, remaining after time t and subject to decay constant λ .

Electromagnetic Transition Probabilities and Weisskopf Estimates

When dealing with electromagnetic transitions, (115) becomes the multipole operator $m_{fi}(\sigma L)$, which determines a transition of proper energy, parity, and multipole order L [35]. With the simple assumption of a proton changing states in the spherical shell model, one may evaluate the transition matrix element by integration over the volume of a nucleus having radius R , such that

$$m_{fi}(\sigma L) = \frac{3}{L+3} R^L, \quad (120)$$

where the angular integral is taken to be unity as a first approximation [35]. The respective transition rates $\lambda(XL)$ for electric E and magnetic M transitions of multipolarity L become

$$\lambda(EL) = \frac{8\pi(L+1)}{L((2L+1)!!)^2} \left(\frac{e^2}{4\pi\epsilon_0\hbar c} \right) \left(\frac{E}{\hbar c} \right)^{2L+1} \left(\frac{3}{L+3} \right)^2 c R^{2L}, \quad (121)$$

$$\begin{aligned} \lambda(ML) = & \frac{8\pi(L+1)}{L((2L+1)!!)^2} \left(\frac{e^2}{4\pi\epsilon_0\hbar c} \right) \left(\mu_p - \frac{1}{L+1} \right)^2 \left(\frac{\hbar}{m_p c} \right)^2 \\ & \times \left(\frac{E}{\hbar c} \right)^{2L+1} \left(\frac{3}{L+2} \right)^2 c R^{2L-2}, \end{aligned} \quad (122)$$

which clearly relate to the classical expression for electromagnetic radiated power

$$P(\sigma L) = \frac{2(L+1)c}{\epsilon_0 L((2L+1)!!)^2} \left(\frac{\omega}{c} \right)^{2L+1} \left(\frac{3}{L+3} \right)^2 (m(\sigma L))^2. \quad (123)$$

The additional terms in (122) are the result of the magnetic multipole operator, which depends on the nuclear magnetic moment of the proton [35]. Together with (121), these equations are known as the Weisskopf estimates. While these estimates do not represent precise calculations, they do provide valuable insights regarding general trends and relative transition rates as functions of

- electric or magnetic character of the transition
- transition energy ε
- transition multipolarity
- nuclear mass number A , by the relationship $R \approx A^{1/3}$

Table 1 lists several transition values as an example of the comparative utility of these estimates. Clearly, upon examination of the table, it is evident transition rates can vary by many orders of magnitude; and one may deduce for nuclear electromagnetic transitions, there is, in general:

- A preference for electric rather than magnetic transitions
- A strong, direct dependence on transition energy
- A strong, inverse dependence on multipolarity
- A relatively weak dependence on nuclear radius

Table 1. Comparison of Weisskopf estimates for the first four electric and magnetic multipole orders. Reproduced from [35].

Multipole Order	Electric	Magnetic
1	$1.0 \times 10^{14} A^{2/3} E^3$	$5.6 \times 10^{13} A^0 E^3$
2	$7.3 \times 10^7 A^{4/3} E^5$	$3.5 \times 10^7 A^{2/3} E^5$
3	$34 \times A^2 E^7$	$16 \times A^{4/3} E^7$
4	$1.1 \times 10^{-5} A^{8/3} E^9$	$4.5 \times 10^{-6} A^2 E^9$

Electromagnetic Transition Selection Rules

The spherical harmonic expansion of the electromagnetic field implies a transition of multipolarity L transfers a quantum of angular momentum equal to $L\hbar$. Conservation of angular momentum consequently requires the vector difference of the initial and final state angular momenta equal the transition angular momentum L . Thus angular momentum transfers between states are restricted according to

$$|J_i - J_f| \leq [L \neq 0] \leq J_i + J_f \quad (124)$$

with the restriction on $L = 0$ indicating the nonexistent monopole transition is forbidden. Additionally, for initial state parity π_i , final state parity π_f , and transition parity $[\pi(XL)]_t$, conservation of parity imposes the constraint

$$\pi_i \pi_f = [\pi(XL)]_t, \quad (125)$$

where

$$[\pi(EL)]_t = (-1)^L, \quad (126)$$

$$[\pi(ML)]_t = (-1)^{L+1}, \quad (127)$$

which are consistent with the classically determined expressions. Informally, the parity constraint states a transition, which changes the parity of the nucleus, requires an odd electric or even magnetic multipole order; whereas a transition, which preserves nuclear parity, requires the opposite. Together, (124) and (125) constitute the selection rules for nuclear electromagnetic transitions. Given these constraints, it is evident there is not in general a one-to-one correspondence between a particular transition from state i to state f and a particular multipole order XL . So long as the XL radiation meets the selection criteria (124), (125), it can “compete” to complete the transition; whence relative rates of competitive XL are given (approximately) by the Weisskopf estimates. In particular, it is common to observe competition between $M1$ and $E2$.

The spherical symmetry assumed in the derivation of (120) limits its applicability to aspherical or deformed systems. In particular, there may exist transitions, for which the necessary change in the angular momentum projection K exceeds the available angular momentum of the multipole order L . However, due to mixing, the selection rule (124) is not strictly applicable to K and the transition is possible. Nevertheless, such $L < \Delta K$ transitions, with the “forbiddenness”

$$\nu = \Delta K - L, \quad (128)$$

are not favored and may proceed at a hindered rate. One may approximate this rate using the empirical relation [51]

$$\log F = \log F_0 + \nu \log f_0, \quad (129)$$

with

$$F = \frac{[\lambda]_{Weisskopf}}{[\lambda]_{experiment}}, \quad (130)$$

and free parameters F_0 and f_0 , which are fit to data.

A theoretical treatment of transition selection in deformed nuclei was completed by G. Alaga in 1955; it reported a similar estimates for f_0 of about 10^{-1} to 10^{-2} [52], consistent with a later empirical determination of Lobner [53]. Alaga applied a second treatment in 1957 to deformation

in the asymptotic limit (77) [54]; whence the collective results of [52, 54] became known as the Alaga rules. In the treatment by Kondev et al, the factor F_0 arises out of a supposition the hindrance has transition multipolarity dependence, which Lobner also suggested [51, 53].

Internal Conversion

In addition to competition among gamma XL radiations, there is also competition between gamma radiation and the internal conversion process, which results in the ejection of an atomic shell electron. Upon completing an internal conversion, an electron leaves the atom with a kinetic energy equal to the difference of the nuclear transition energy and the atomic shell binding energy. Thus, the kinetic energies are variable, owing to the differing atomic shell energies. However, despite this variability, the discrete nature of both the atomic and nuclear transition processes ensures the resulting electron spectrum consists only of discrete components [35]. Vacancies left by converted electrons are filled with atomic electrons from higher shells in radiative transitions, which produce characteristic X -rays. These characteristic X -rays are frequently present in the low-energy gamma spectra of nuclear radiation.

Assuming a nuclear transition of known energy, the kinetic energy of the electron indicates the shell of origin, leading to the labeling convention, in which K, L, M, \dots correspond to the primary atomic oscillator shells $n = 1, 2, 3, \dots$. According to this convention, one also might identify the subshell of origin with a Roman numeral subscript (i.e. L_I).

Competition between gamma emission and internal conversion necessitates correction for the latter when using gamma measurements to determine state lifetimes or transition intensities. Generally, the total decay constant for the gamma and internal conversion processes of a given transition are additive, according to

$$\lambda_t = \lambda_\gamma + \lambda_e, \quad (131)$$

where the subscripts t , γ , and e , respectively indicate *total*, *gamma*, and *electron*. Conventionally, the internal conversion coefficient α is the relative rate of electron emission to gamma emission,

$$\alpha = \frac{\lambda_e}{\lambda_\gamma}, \quad (132)$$

such that

$$\lambda_t = \lambda_\gamma(1 + \alpha). \quad (133)$$

Partial conversion coefficients, representing contributions from the different atomic shells are additive; and one typically labels them with the shell as a subscript.

Aside from differences in wave functions, one calculates internal conversion transition rates in the same manner as gamma transitions, according to Fermi's Golden Rule (114). Using such calculations, and the comparable calculations for gamma emission, one can formulate a rough, general expression for the conversion coefficients of XL multipolarity:

$$\alpha(EL) = \left(\frac{Z}{n}\right)^3 \left(\frac{L}{L+1}\right) \left(\frac{e^2}{4\pi\epsilon_0\hbar c}\right)^4 \left(\frac{2m_e c^2}{E}\right)^{L+5/2} \quad (134)$$

$$\alpha(ML) = \left(\frac{Z}{n}\right)^3 \left(\frac{e^2}{4\pi\epsilon_0\hbar c}\right)^4 \left(\frac{2m_e c^2}{E}\right)^{L+3/2} \quad (135)$$


Values of α are hardly bounded, ranging over many orders of magnitude. Further applying the expressions (134) and (135), it is possible to deduce qualitatively the important phenomenology of internal conversion. Specifically in terms of α , one observes:

- A direct proportionality with Z^3
- A direct relation with multipole order
- An inverse relation with transition energy
- An inverse proportionality with the number of the atomic oscillator shell, given by n^{-3}

One therefore expects conversion will be especially strong at low energies, in K -shells of heavy nuclei [35]. Additionally, due to preclusion from the radiative process, $E0$ transitions proceed entirely through conversion channels and only can be detected accordingly.

Gamma Decay Cascades

A nucleus in an excited state is unstable against radioactive decay of some form; and when the excitation is insufficient for particle emission, the ensuing de-excitation must be electromagnetic

in nature. At a level of excitation such that many intermediate, distinct states exist between the excited state and ground state, the decay most often proceeds via a cascade through the intermediate levels, in accordance with the selection rules (124) and (125). While it is possible for an electromagnetic decay to proceed directly to the ground state, this is usually not the case, particularly if the selection rules preclude  Moreover, any number of subsequent states may be available to participate in the transition from a given excited state. Due to this competition among possible transitions at each stage of a cascade, the precise path of the decay is not, in general, predictable for an individual nucleus. Instead it is a stochastic process, for which the decay of many nuclei determines probabilities or branching ratios at each branch point. This is the essence of a statistical cascade.

In the event the nucleus also has substantial angular momentum, the yrast line represents a boundary at which a statistical cascade must assume a bias favoring angular momentum reduction. Thus, if the energy difference between an excited state and the underlying yrast state is less than that required for particle emission, the decay proceeds through statistical gamma cascade to the yrast region [55]. The absence of levels below yrast then forces the gamma decay down the yrast line, shedding angular momentum in the process. Consequently, a single state (or a few nearby states with the same angular momentum) collects most of the population decaying from states with angular momenta higher than its own [55]. This phenomenon is characteristic of an yrast cascade, which Figure 15 illustrates alongside the statistical cascade to demonstrate the distinction. Given the definition of the yrast line according to (60) it is evident yrast cascades follow rotational bands in rotating nuclei. However, as previously discussed, these bands may “cross” for various reasons and the cascade will settle into the lowest energy band at a given angular momentum.

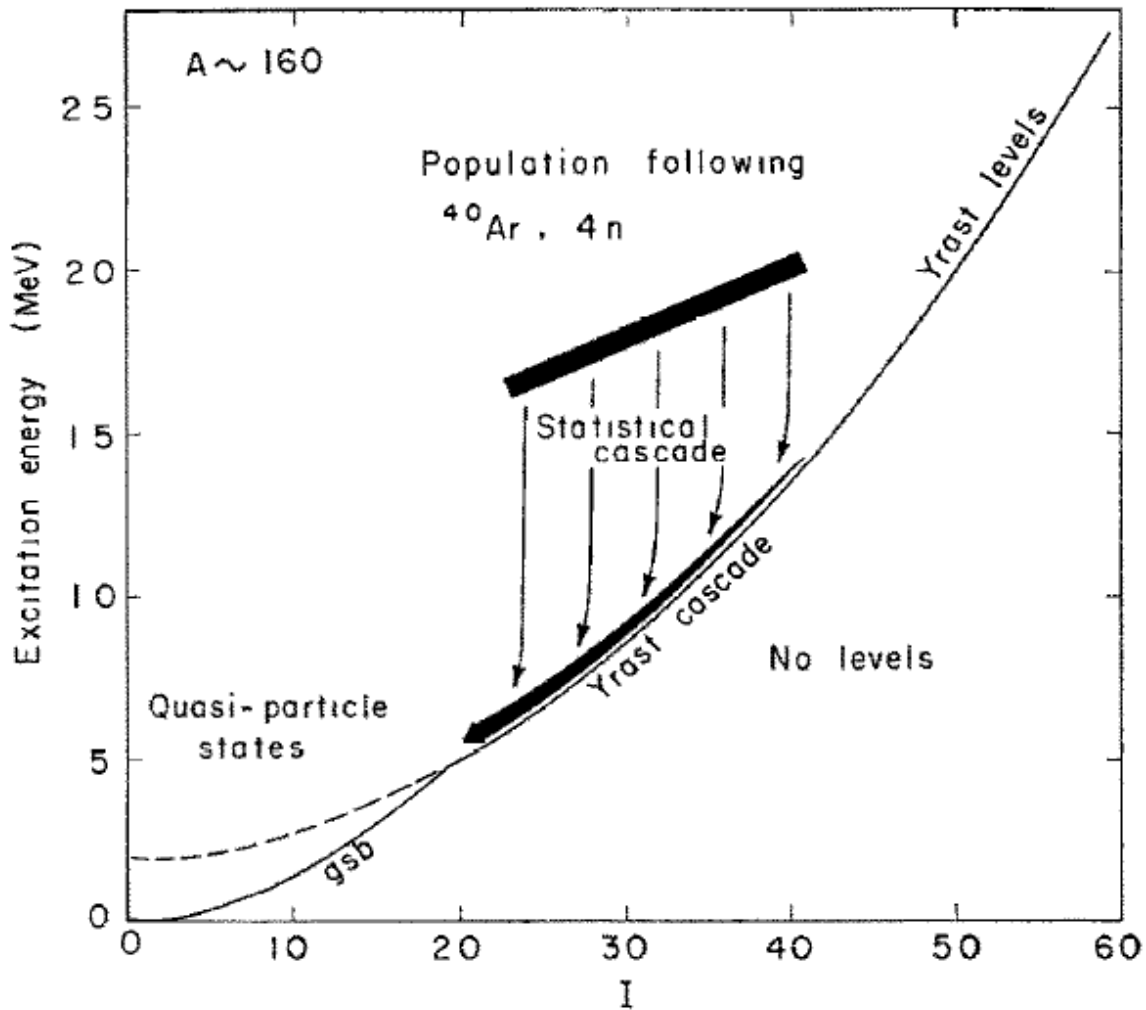


Figure 15. Notional diagram illustrating the distinction between statistical and yrast cascades from levels populated in a hypothetical $^{124}\text{X}(^{40}\text{Ar},4n)^{160}\text{X}$ reaction. Reproduced from [56]

Metastable Excited States

Excited states, which experience significant hindrance in their decay, are considered metastable if the lifetime exceeds a certain threshold. It is common to refer to such states as isomers. There is no consensus on the threshold for isomer lifetimes but as general trend, the literature cites one nanosecond [57]; whereas Jain et al. quote ten nanoseconds in the *Atlas of Nuclear Isomers* [57]. As of 2015 there were 2469 isomers, whose lifetimes ranged between the ten nanosecond threshold and about 10^{15} years [57]. Several structural mechanisms can hinder decays to produce long lifetimes; and isomers are classified accordingly. The literature acknowledges four (or perhaps five) isomer categories.

- Spin isomers result from a state, which has no path to the ground state, except through a high-multipolarity transition, which requires a large change in angular momentum. Such transitions are obviously restricted according to the Weisskopf estimates, leading to a low probability of decay.
- *K*-isomers result from states, whose only available transitions have a significant value of ν in (128) and are consequently *K*-forbidden or, more precisely, *K*-hindered.
- Shape isomers arise from a potential minimum or well created by the shape of a substantially elongated nucleus. They can decay back to the ground state via gamma decay; or possibly “free” themselves by tunneling [34].
- Fission isomers are essentially shape isomers, which can decay through fission or gamma decay to the ground state well. Either process may involve tunneling.

Figure 16 and Figure 17 provide a pictorial representation for the sources of isomerism and notional level schemes as they relate to the four different categories. A fifth category, identified as seniority isomers, seems to exist as a consequence of broken nucleon pairing in semi-magic nuclei [57].

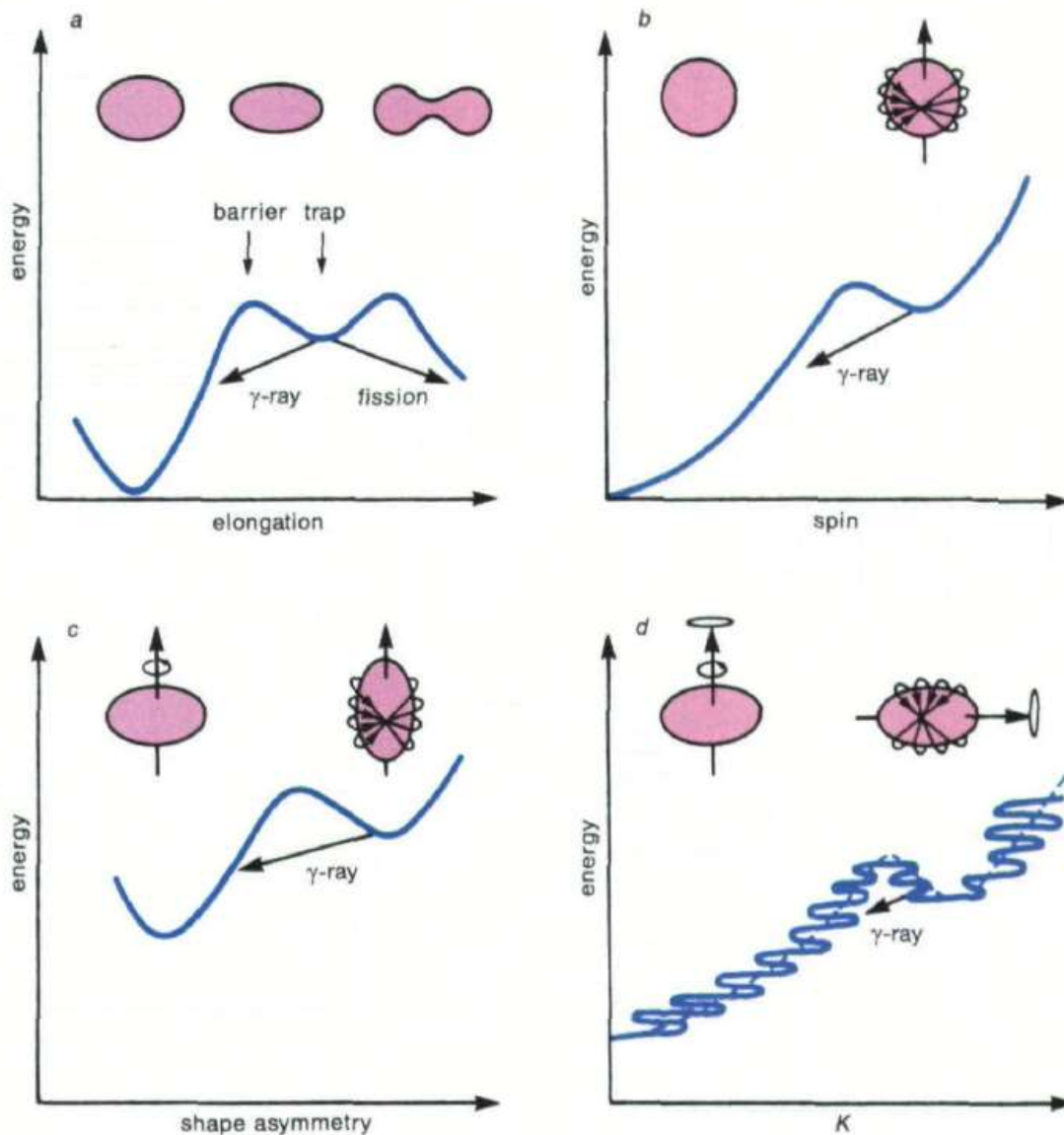


Figure 16. Simple pictorial representations for the causes of isomerism. Reproduced from [2].

As already suggested, isomer decay may proceed through a number of channels. Most commonly decay occurs through an electromagnetic transition, commonly referred to as isomeric transition or IT. However, other modes, depending on isomer category are possible, including beta decay, beta-delayed neutron decay, beta-delayed proton decay, alpha decay, and spontaneous fission

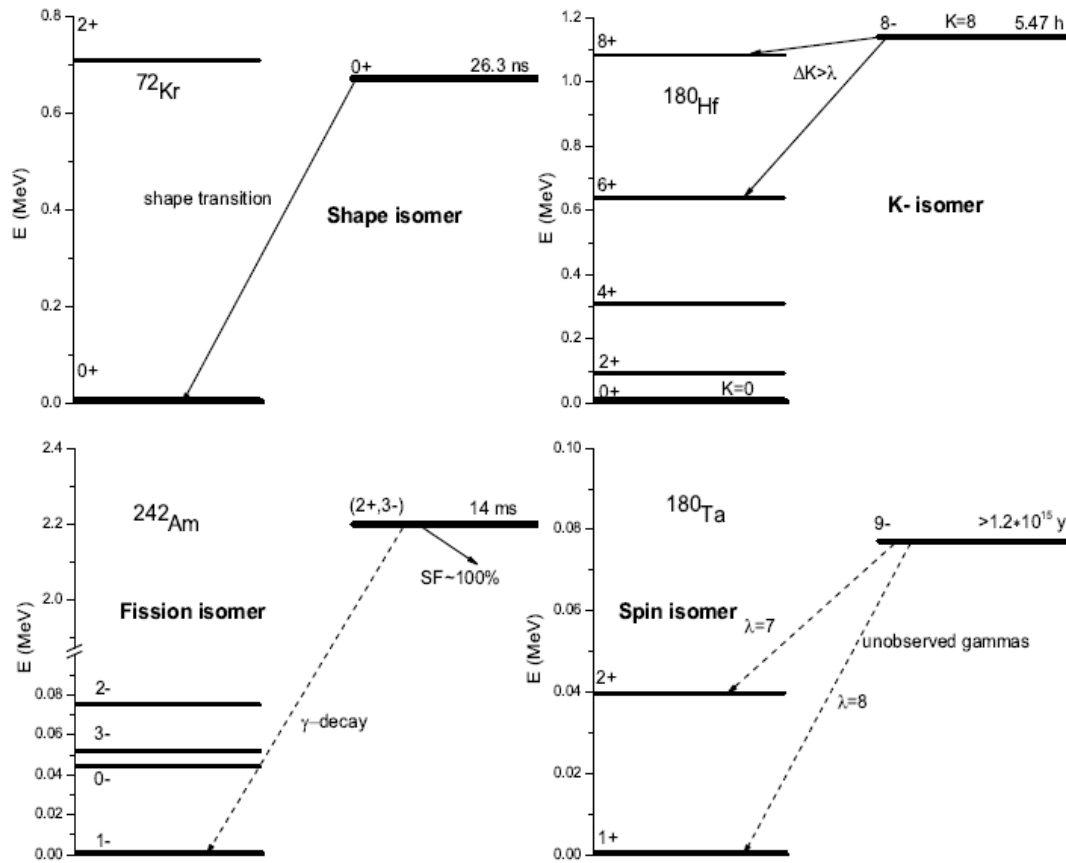


Figure 17. Schematic diagram illustrating the isomer categories in a hypothetical level scheme. Reproduced from [57].

Nuclear Reactions

Nuclear reactions provide a crucial tool for probing nuclear structure; but no single reaction is generally applicable to the investigation of all structural phenomena. A wide array of energies and angular momenta are needed to characterize a nucleus, necessitating proper selection of reaction mechanisms to meet experimental objectives.

Definition

A nuclear reaction involves the interaction of two or more distinct reactant nucleon bodies through the nuclear or Coulomb forces. The interaction may appreciably alter (1) the reactants, creating new, distinct products; (2) reactant trajectories, scattering the incident and target reactants, or (3) more generally, some combination thereof. One formally defines a reaction according to

$$a + X \rightarrow Y + b \quad (136)$$

or more compactly

$$X(a, b)Y . \quad (137)$$

Typically, in the context of an experiment, X represents the target and a the projectile; whereas Y is a heavy product, which is usually confined to the bulk of the target material, and b is a light product, which escapes the target and interacts with a detector. In general, b may be a particle, a gamma ray, or both; but often in reactions, where gamma emission is implicit, the notation omits reference to the gamma(s).

Classification

Classification of reactions, in which the reactants and products differ, is a function the interaction between the projectile and target. In one extreme are the direct reactions, which involve only a subset of the nucleons – perhaps only a single nucleon of the projectile and the outermost valence nucleon of the target. Direct reaction timescales are very short, on the order of 10^{-22} seconds, and correspond to the time the reactants are in direct contact [35]. The other extreme involves a complete redistribution of the projectile energy among all target and projectile nucleons. Thereupon results a compound nucleus, in a state akin to thermal equilibrium, and whose excess energy, through random fluctuation, may concentrate sufficiently in a subset of nucleons to allow their separation from the whole, in a process akin to evaporation. One often denotes, in the reaction definition (128), formation of a compound nucleus as an intermediate state C^* such that

$$a + X \rightarrow C^* \rightarrow Y + b . \quad (138)$$

Timescales for compound nucleus reactions are on the order of 10^{-16} seconds and, in comparison to direct reactions, reflect the time necessary for thermalization and subsequent evaporative separation of the product(s).

Between the compound nucleus and direct reaction, there exists a region of resonance reactions, in which the reactants form a quasibound state prior to separation of the products [35]. Conceptualized in terms of the projectile de Broglie wavelength, which is inversely related to

kinetic energy, it is evident the length-scale of interaction is also inversely related to energy [35]. Qualitatively then, reactions tend toward compound nucleus formation as energy decreases; whereas higher energies favor direct reaction mechanisms.

Energetics and Thresholds

The analysis of nuclear reactions is dependent on conservation relations, as it is with any physical system. Not surprisingly, in a reaction the following quantities are invariant:

- Proton count
- Neutron count
- Total Linear momentum
- Total Angular momentum
- Total Energy
- Parity

In terms of the relativistic kinetic energies and rest masses, conservation of total energy dictates for the reaction (138),

$$m_X c^2 + T_X + m_a c^2 + T_a = m_Y c^2 + T_Y + m_b c^2 + T_b , \quad (139)$$

with kinetic energy T and mass m . One now defines for the reaction the Q -value, equal to the surplus or deficit of product kinetic energies to reactant kinetic energies; whence

$$Q = T_Y + T_b - (T_X + T_a) . \quad (140)$$

This is equal to the difference of the reactant and product rest masses, according to

$$Q = (m_X + m_a - (m_Y + m_b))c^2 . \quad (141)$$

As energy is lost or gained, respectively, in the creation or annihilation of mass, negative Q -values represent an endothermic process; whereas positive Q -values represent an exothermic process.

Conservation of linear and angular momentum also dictates a two-body reaction must occur in a plane, necessitating, in the x and y -directions, the respective conservation conditions

$$p_b \cos \theta + p_y \cos \phi = p_a , \quad (142)$$

$$p_b \sin \theta - p_y \sin \phi = 0 . \quad (143)$$

Upon elimination of the unobserved quantities in Y and ϕ , the momentum conservation conditions and the energy conservation condition (139) determine the relationship

$$\begin{aligned} T_b^{1/2} &= \left(\frac{m_a m_b T_a}{(m_Y + m_b)^2} \right)^{1/2} \cos \theta \\ &\pm \left(\frac{m_a m_b T_a \cos^2 \theta + (m_Y + m_b)(m_Y Q + (m_Y - m_a)T_a)}{(m_Y + m_b)^2} \right)^{1/2} . \end{aligned} \quad (144)$$

Importantly, for $Q < 0$ there exists at $\theta = 0$ the threshold condition,

$$[T_a]_{threshold} = |Q| \frac{m_Y + m_b}{m_Y + m_b + m_a} , \quad (145)$$

which sets, on the kinetic energy of the projectile, a lower limit necessary for the reaction to proceed [Krane].

Cross Sections and Excitation Functions

Optimization of the experiment for data collection demands one select the projectile kinetic energy, which maximizes output of the desired product(s). In general, a reaction between a given target-projectile pair may proceed through one of several possible channels, each generating a unique set of products; although different channels may share certain products in common. A single reaction is also a stochastic process, whose outcome or channel is unpredictable; and only over many reactions is the probability of a particular reaction channel quantifiable. Most often, one expresses this probability as a partial reaction cross section σ_b according to

$$\sigma_b = \frac{R_b}{I_a N} , \quad (146)$$

where R_b is the production rate of b , I_a is the current of the projectile a , in particles per unit time, and N is the number of target reactants X , per unit area. Whereas a probability is of course unit-




less, the cross section accounts for the continuum of physical space through which the reactants interact. It clearly has units of area, usually given in barns (b), which are equivalent to 10^{-28} m^2 . The true probability relates to the total (not partial) cross section through the expression

$$\frac{I_a(x)}{I_a(0)} = \exp(-\sigma n x) = 1 - P(x), \quad (147)$$

where n is the number density of target reactants, x is the distance along the current path, and $P(x)$ is the cumulative probability of reaction as a function of x .

The partial cross sections are additive, and their sum gives the total cross section over all channels for a given projectile-target pair. In the case of a particular product the cross section becomes the sum of the individual cross sections for each channel leading to the desired product. However, in practice one usually measures only the product of interest and so determines the product cross section over all available channels. Generally, cross sections have both energy and angular dependence; but for the purposes of this research, only the energy dependence, is of concern. One typically refers to this energy dependence as an excitation function; and its maximum determines the projectile kinetic energy, which maximizes output of the desired product.

Synopsis of Ir-192 Research


McMillan et al. in 1937 identified Ir by irradiating a Ir target with neutrons generated from a deuteron beam incident on lithium [14, 15]. As of 2012, observation was confirmed for thirty-seven other iridium isotopes, ranging from isobars 165 through 202; and an additional 63 isotopes from isobars 155 through 261 were predicted to be observable with half-lives greater than one nanosecond [15]. Given that ^{192}Ir lies in the middle of this range and between the two stable iridium isotopes at isobars 191 and 193, one may consider it neither neutron nor proton rich llowing its discovery, and through the present, ^{192}Ir became the object of several research efforts to measure its nuclear properties and explore its structure.

NSR, ENSDF, and XUNDL Summary

Among the research databases, which BNL maintains under its NNDP mandate, is the Nuclear Science References (NSR). The NSR compiles titles and web links (where available) of

publications in nuclear science from more than 80 journals extending back to 1896 [16]. As of 17 June 2017, an NSR query for ^{192}Ir yields 410 publications dated from 1950 to the present. Drawing from this corpus and elsewhere, C. Baglin completed, on 15 Jun 2012, the most recent evaluation of ^{192}Ir data for the ENSDF database [1]. This evaluation incorporates several publications, from 1959 to 2007, detailing investigations into ^{192}Ir structure via gamma spectroscopy and direct reaction mechanisms. Table 1 summarizes these experiments, which form the basis of the ENSDF adopted level scheme. A number of additional publications, dated from 1937 to 2012 inform present ENSDF determinations of ^{192}Ir ground state measurements, including the magnetic dipole moment, electric quadrupole moment, half-life, and isomeric numerous transition lifetimes.


Table 2. Summary of nuclear structure experiments incorporated into the 2012 ENSDF evaluation for ^{192}Ir .


Reaction	Energy	Measured	Instrument	Author	Year
$^{191}\text{Ir}(n,\gamma)^{192}\text{Ir}$	Thermal	E- γ , I- γ	Ge(Li)-pair-scin-spect	H. Kruger	1971
$^{191}\text{Ir}(n,\gamma)^{192}\text{Ir}$	Thermal	E- γ , I- γ	Pair spectrometer	J. Kern	1991
$^{191}\text{Ir}(n,\gamma)^{192}\text{Ir}$	2 keV	E- γ , I- γ	Pair spectrometer	J. Kern	1991
$^{191}\text{Ir}(n,\gamma)^{192}\text{Ir}$	4 keV	E- γ , I- γ	Pair spectrometer	J. Kern	1991
$^{191}\text{Ir}(d,p)^{192}\text{Ir}$	15, 22 MeV	$d\sigma/d\Omega$	Q3d spectrog, scin	J. Kern	1991
$^{193}\text{Ir}(d,t)^{192}\text{Ir}$	14, 15, 22 MeV	$d\sigma/d\Omega$	Q3d spectrog, scin	J. Kern	1991
$^{191}\text{Ir}(d,p)^{192}\text{Ir}$	16 MeV	$\sigma(\theta)$	Mag spectrograph	P. Garrett	1994
$^{193}\text{Ir}(d,t)^{192}\text{Ir}$	18 MeV	$\sigma(\theta)$	Mag spectrograph	P. Garrett	1994
$^{193}\text{Ir}(^3\text{He},\alpha)^{192}\text{Ir}$	25.5 MeV	$d\sigma/d\Omega$	Mag spectrograph	P. Garrett	1994
$^{195}\text{Pt}(p,\alpha)^{192}\text{Ir}$	18 MeV	$d\sigma/d\Omega$	Mag spectrograph	P. Garrett	1994
$^{191}\text{Ir}(n,\gamma)^{192}\text{Ir}$	Resonance	E(res)		S. Mughabghab	2006
$^{191}\text{Ir}(n,\gamma)^{192}\text{Ir}$	Thermal	E- γ , I- γ	Ge(Li)  spectrometer	H. Choi	2007

Upon review of the ENSDF for ^{192}Ir , it is evident there are a few foundational publications, which contribute significantly, both in data and analysis, to the present understanding of ^{192}Ir structure. These are: J. Kern et al. (1991), P. Garrett et al. (1994), and M. Balodis et al. (1997)[†] [17, 18, 19]. Having missed the 2012 evaluation cutoff, a second publication by M. Balodis et al. [8] serves as the source of an updated but unevaluated level scheme in the XUNDL [20]. Nevertheless, it contains substantive ^{192}Ir structural insight.

[†] The AFIT Research Librarian was able to locate only one copy of this publication, which exists at a library in Slovenia. In the absence of an interlibrary lending agreement with European libraries, it may be inaccessible to us.

J. Kern et al.

J. Kern et al. in 1991, performed the series of experiments, listed in Table 1, to probe the structure of ^{192}Ir . Acquired data collectively enabled composition of a level scheme up to  Subsequent, qualitative interpretation of the level scheme relied upon the rotor-plus-particle model, which suggested the presence of several rotational bands. Meanwhile, the interacting boson-fermion-fermion model (IBFFM) facilitated calculations for quantitative comparison with experimental results.

The ^{191}Ir neutron capture experiments relied on: (1) a 3 cm^3 Ge(Li) pair spectrometer, with a 5 keV full-width half-maximum (FWHM) resolution at 6 MeV for observation of primary transitions; (2) a 3 cm^3 Ge(Li) spectrometer in Compton anticoincidence mode, having a 1.6 keV FWHM at 100 keV, in conjunction with a curved crystal spectrometer in DuMond geometry, for observation of secondary transitions; (3) a magnetic spectrograph with respective resolutions of 0.19% and 0.06% at 30 and 190 keV for observation of conversion electrons; and (4) a HPGe-Ge(Li)  spectrometer with 35 nanosecond FWHM time resolution and 2.5 keV energy resolution at 100 keV, for gamma coincidence measurements. In total, the neutron capture spectra revealed 118 primary transitions, in the range of 4640 to 6200 keV and approximately 250 to 300 secondary transitions in the range of 48 to 635 keV.

Given the various modalities of measurement, Kern et al. were able to make significant contribution to the ^{192}Ir level scheme. They also made efforts to interpret their findings in terms of both a rotor-particle model and the interacting boson fermion fermion model (IBFFM). Whereas they claim reasonable success with the latter, M. Balodis, in more recent publications, argues in favor of the TQPRM and offers theoretical predictions to that end. New experimental, spectroscopic data should provide a valuable test of that position. As far as is evident from the literature, the efforts of J. Kern et al. were the last to complete any substantive gamma spectroscopy for ^{192}Ir .

P. Garrett et al. 

P. Garrett et al. used a magnetic spectrograph and photographic plates to analyze and record the products from (d,t), (d,p), (^3He , α), and (p, α) reactions, which generated ^{192}Ir . Deuterons in the (d,t) reaction were at 18 MeV, giving an energy resolution (FWHM) of 5.7 keV; whereas those

in the (d,p) reaction were at 10 MeV, giving an FWHM of 8.9 keV. The ^{192}Ir and protons respectively had energies of 25 MeV and 18 MeV. Spectra were recorded at multiple angles, relative to the beam axis, to determine the angular distribution of the reaction cross section; and the results were fitted to theoretical predictions based on the Distorted Wave Born Approximation (DWBA). This analysis enabled deduction of nuclear level energies, parities, spectral intensities, and possible spin values up to about 1 MeV excitation.

Experimental results were compared with predictions of the Nilsson Model and the IBFFM. IBFFM calculations were found to agree with the empirical data in terms of the level density below about 500 keV of excitation; but predictions for the energies of certain low-lying states were frequently high. Interpretation based on the Nilsson model met with similar results. In particular, the absence of the predicted $K^\pi = 6^-$ band-head below the $K^\pi = 3^-$ band-head implies an apparent violation of the Gallagher-Moszkowski rule. The authors suggest this, in addition to other poorly-predicted transitions is a consequence of complex or dynamic deformations, for which the model fails to account.

Others

The works of F. Tarkanyi [21] and K. Hilgers [22] are of particular interest for their respective measurements of (d,2n) ^{192}Ir and (p,n) ^{192}Ir excitation functions. Both provide data useful in the selection of beam energies in the coming experiments.

Present ENSDF Data and Measurements

^{192}Ir ground state properties, for which the ENSDF includes a determination, are: half-life, decay energy, decay branching, magnetic and electric moments, and spin-parity assignment. The half-life value of 73.829 days is the result of a weighted average over seven measurements taken from 1961 to 1992. [1] Mean β^- decay energy of 1454.5(24) keV is the result of three measurements from 2003 to 2012 [1]. Measurements for the gamma and conversion electron intensities of the excited ^{192}Os and ^{192}Pt decay products fix the respective branching fractions at 4.76(4)% (ϵ) and 95.24(4)% (β^-) [1]. The magnetic dipole moment is given as 1.924(10) based on a measurement of the magnitude made in 1989, using nuclear magnetic resonance (NMR) [1], and a gamma polarization measurement, which determined the sign in 1988 [1]. The electric

quadrupole moment of 2.22(7) is the average of two (NMR) measurements made in 1996 and 1989 [1].

Several sources facilitate deduction of the Nilsson configuration and 4^+ spin-parity assignment for the ground state. Atomic beam measurements of W. Doyle et al. in 1963 fix the magnitude of the spin at $I = 4$ [23]; while observation of the electric octupole (E3) gamma transition, from the negative parity, 57 keV ($m1$) isomer level to the ground state, demands a positive parity [1]. (Note the ENSDF evaluation does not explicitly specify any reference or deduction, which establishes the negative parity of the 57 keV level. However, the ENSDF data do include a primary gamma transition from the $1^+, 2^+$ neutron capture state at 6,198 keV directly to the 57 keV level, which has a spin assignment of 1. Thus, it is conceivable this transition consists of a mixture of electric dipole (E1) and magnetic quadrupole (M2) multipolarities, which would result in the correct parity at 57 keV.) Doyle et al. also postulated a Nilsson configuration of $3/2[402]$ for the odd (77^{th}) proton but could not deduce a compatible configuration for the odd (115^{th}) neutron due to theoretical and empirical limitations at the time [23]. With additional data and theoretical advances, J. Kern et al. (1991) were able to resolve this discrepancy by postulating the probable mixed Nilsson configuration $((\pi 3/2[402])-(\nu 11/2[615])) + ((\pi 11/2[505])-(\nu 3/2[512]))$ [1, 17].

Based on the available spectroscopic and reaction data, the ENSDF identifies 288 levels for ^{192}Ir above the ground state [1]. About half of these (146) are fed, at least in part, by primary transitions from the 6198.13(11) keV $^{191}\text{Ir}(n,\gamma)^{192}\text{Ir}$ neutron capture state, which G. Audi measured in 2011 [24]. The highest observed state below the neutron capture state is at 1703.0(7) keV, while the highest state with a spin-parity assignment is at 1050.53(15) keV. Existing data do not support spin-parity deduction for any of the approximately seventy observed intervening states [1]. The highest state with any confirmed secondary transitions lies at 508.988(8) keV; and, consequently, most of the known structure in the level scheme lies below this energy. Spin values of the observed states range from zero to six, excluding the spin eleven $m2$ isomer.

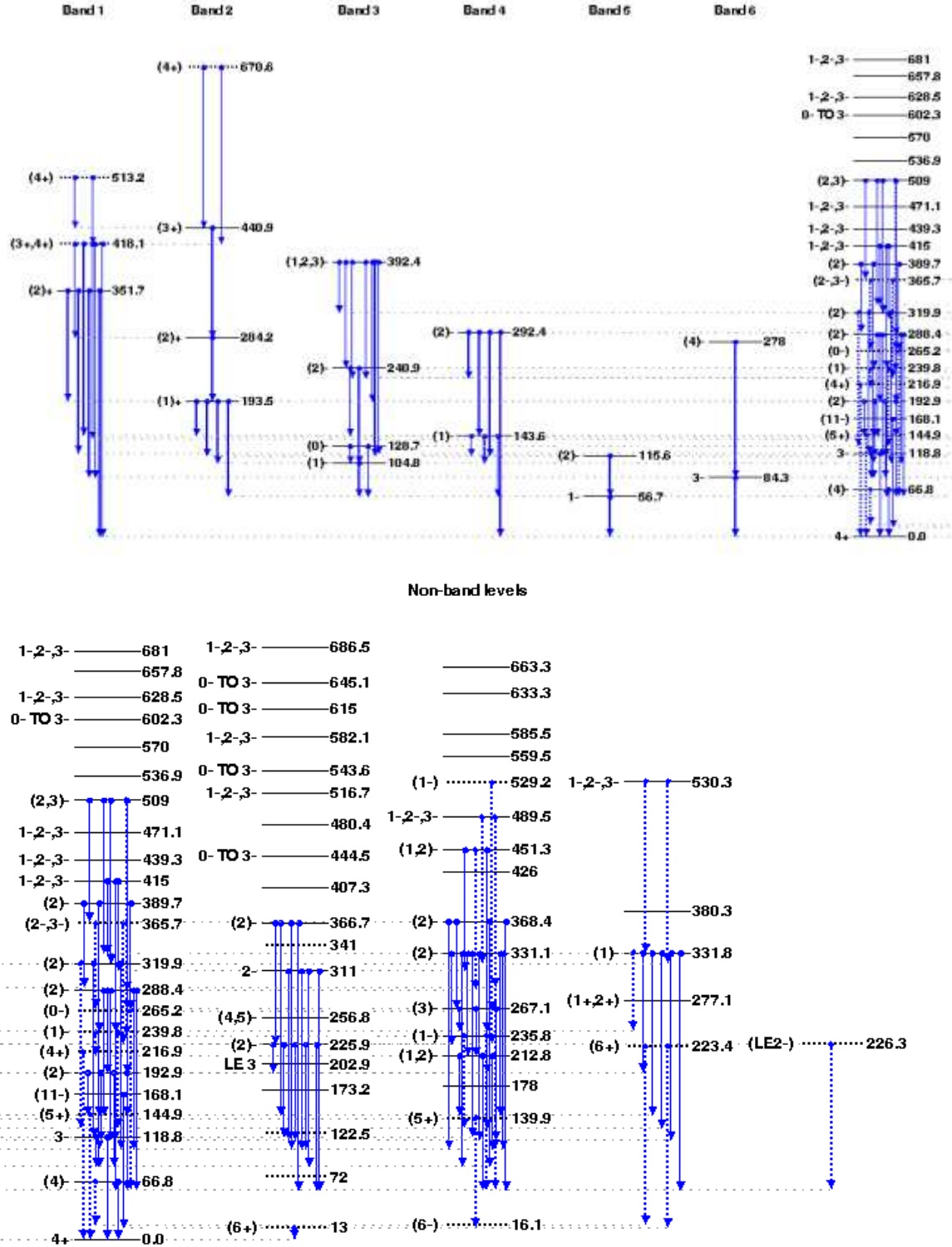


Figure 18. Subset of the ^{192}Ir adopted level scheme (up to 700 keV) based on data residing in the ENSDF. The present theoretical paradigm interprets the level-scheme primarily in terms of rotational bands (shown in the figure on top) built on two-quasiparticle Nilsson configurations. Transitions in the lower figure are not known to be associated with band structure. The right-most column in the upper figure is provided for its reference to the ground state. It is the same as the right-most column in the lower figure and does not represent a rotational band. From [31].

Excluding the ground state, ^{192}Ir has seven known states with lifetimes longer than one nanosecond. In particular, these include the m1 isomeric state at 57 keV, with a half-life of 1.45(5) minutes and the m2 isomeric state at 168 keV, with a half-life of 241(9) years. For reference, Table 2 summarizes each of the long-lived states. It is interesting to note observed decay pathways for most of these states have low (E1, M1) multipolarities.

The determination of the m1 isomer half-life incorporates measurements from G. Weber in 1953 and 1954 [25, 26]; and transition multipolarity measurements come from J Mize in 1954 and R. Gehrke [27, 28]. The m1 isomer decay includes an isomeric transition (IT) component (99.9825%), which results in γ emission, and a β^- component (0.0175%) to ^{192}Pt . In an effort to establish the spin assignment of the m1 isomer, G. Scharff-Goldhaber et al. made a measurement, which confirmed the presence of the β^- component and determined its branching fraction, in 1959 [29]. The existing level scheme indicates feeding of the m1 isomer through nineteen transitions (fifteen confirmed), ranging in energy from 105 keV to 6198 keV, and a single γ emission, resulting from IT directly to the ground state.


Table 3. List of ^{192}Ir states with half-lives exceeding one nanosecond. Data from [1].

State (keV)	J^π	$T_{1/2}$	Decay	Fed by (unc)	No. of decay γ s (min XL)
56.72	1^-	1.45(5) min	γ (99.9825%), β^- (0.0175%)	19 (4)	1 (E3)
66.83	4^-	15(4) ns	γ	1 (1)	1 (E1)
84.275	3^-	1.9 ns	γ	9 (1)	1 (E1)
104.776	$(1)^-$	17.4(26) ns	γ	15 (1)	1 (M1+E2)
118.7824	3^-	>15 ns	γ	6	2 (E1)
168.14	$(11)^-$	241(9) y	γ	0 obs	1 (E5)
193.511	$(1)^+$	2.7(6) ns	γ	3	4 (E1)

There exists no observation of a β^- decay component for the m2 isomer; and due to decay energy restrictions, the highest accessible spin in ^{192}Pt would be seven [1]. Consequently, the decay is known to proceed entirely by IT; and determination of its half-life relies on the measurements of G. Harbottle in 1970 [30]. Present ENSDF data suggest a transition of 155 keV, to a “highly tentative” 13 keV level with 6^+ spin-parity, depopulates the m2 state [1]. This implies the tentative transition multipolarity of E5. Naturally, one might expect such a transition should be highly converted; and indeed, the listed internal conversion coefficient is 1085. There is also no observation of a transition feeding the m2 isomer; although, this is likely due to the low-spin excitation of the (n,γ) reactions, from which most of the gamma spectra were acquired. G.

Scharff-Goldhaber et al. reported, in 1959, the m2 isomer excited state energy and multipolarity as 161(5) keV and E5, respectively, and then in 1977 identified the 155 keV transition associated with the isomer decay [29, 32]. While J. Kern et al. observed a 155 keV transition in the thermal neutron capture spectrum, it was not situated in the level scheme until M. Balodis et al. deduced its role in the complete m2 isomer decay pathway in 1997 [19]. Completion, to the ground state, of the ensuing transition necessitates placement of the tentative 6^+ , 13 keV level, whose existence was a subject of speculation by G. Scharff-Goldhaber et al. [29]. This proposed sub-scheme is also contingent on the tentative 11^- spin-parity for the isomer, based on probable proton-neutron Nilsson configurations. As of 2014, M. Balodis et al. report confirmation for both the 11^- spin-parity of the isomer and the existence of the 13 keV, 6^+ state, according to a Nilsson model interpretation of the odd nucleon states and rotor-plus-quasiparticle coupling calculations. [8]. However, there is not yet any empirical data, which captures the 13 keV transition feeding the ground state. Observation of this transition would likely be difficult, given its predicted internal conversion coefficient of 5.7×10^4 , and E5-hindered depopulation of the isomer. Nevertheless, the unevaluated level scheme in the XUNDL indicates several transitions, which may provide additional feeding.

M. Balodis and T. Krasta

M. Balodis et al. reanalyzed, in 2014, ^{192}Ir neutron capture and particle transfer reaction data, which was acquired, predominantly, through the experiments of J. Kern et al. in 1991 and P. Garrett et al. in 1994. Generally, this analysis sought to provide a consistent structural picture of the ^{192}Ir nucleus based on the most recent insights. Specific objectives included evaluation of the existing Nilsson configuration band heads and identification of new band heads, with associated rotational levels. These analyses were accomplished according to the rotor-plus-quasiparticle coupling (RPC) framework and the Gallagher-Moszkowski (GM) rule. The authors also posed a question regarding the relative deformities of ^{192}Ir and ^{194}Ir , offering the hypothesis ^{192}Ir has the greater deformity, leading to more regularity in the level scheme. 

Re-evaluation of the average resonance capture (ARC) data of J. Kern et al. permitted placement, in the level scheme, of 44 previously observed but unincorporated transitions, including the 155.16 keV decay transition from the 168 keV, m2 isomer. Relocations for eight previously incorporated transitions were also necessary to maximize level scheme internal consistency.

Band structure analysis then required application of the GM rule for identification of two-quasiparticle proton-neutron configurations. Use of the three lowest proton and four lowest neutron Nilsson orbits from neighboring odd-isobar nuclei, enabled composition of 24 such configurations. Fits of the level energies, in the newly modified level scheme, to the two-quasiparticle spins and spin projections, yielded bands or band heads for 21 of the 24 configurations. According to the authors, in addition to generating a more internally consistent level scheme, the new band structure enabled confirmation of the 168 keV, m2 isomer spin-parity and 13 keV, 6^+ level, which the isomer populates through the known 155 keV transition. In their concluding remarks, the authors articulated the need for additional experimental data, particularly gamma coincidence measurements, to support their findings. Note, however, while promising or useful, these findings are not yet part of the evaluated data set for ^{192}Ir . Figure 20 and Figure 19 present the proposed rotational band additions to the present level scheme.

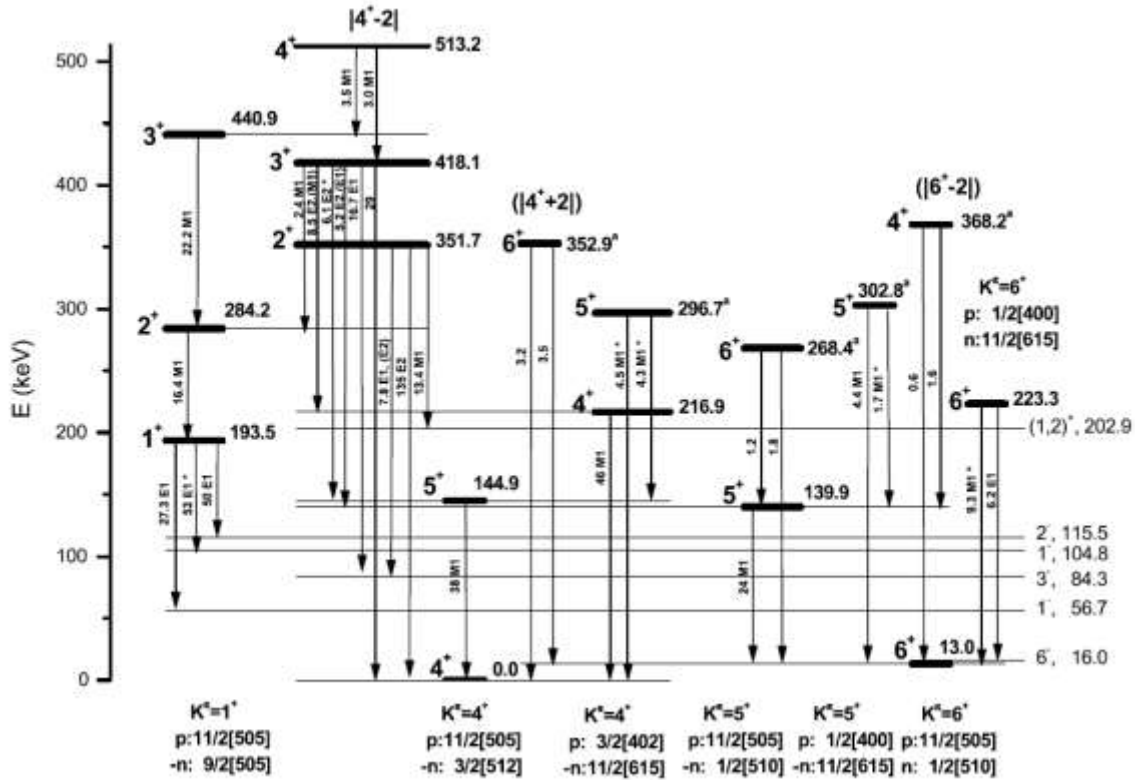


Figure 19. Proposed new positive parity bands (set one) for ^{192}Ir . From [Balodis 2014]



IV. Experiment

Conceptually, a description of the experiment is straightforward. One uses a nuclear reaction, which creates the desired nuclide in an excited state; and the gamma radiation, emitted during the subsequent decay, carries energetic and temporal information about the relationships among the various levels of excitement. Measurement of this radiation, and application of various analyses to the resulting data, enables partial reconstruction of the underlying structure, which one usually represents as a level scheme.


Reactions

This research will employ, in sequence, the following reactions:

- $^{192}\text{Os}(\text{d},2\text{n})^{192}\text{Ir}$
- $\{^{192}\text{Os}(7\text{Li},\alpha 3\text{n})^{192}\text{Ir}\}^{\ddagger}$
- $^{192}\text{Os}(\text{p},\text{n})^{192}\text{Ir}$



Rationale

Experimental objectives dictate investigation over a range of energy and angular momentum excitation for the ^{192}Ir nucleus. In particular, there is interest in examining high-spin states, since only lower spin states ($\leq 6\hbar$) have been observed to date [1].  The experiment campaign commences with the (d,2n) reaction to explore the spin and energy excitation in an intermediate range. Analysis of the (d,2n) data should provide, with respect to ^{192}Ir structure, valuable insights, which can then guide the experiment parameters and data collection for the subsequent ^7Li reaction.

Due to their capacity for large angular momentum and energy transfer, heavy-ion, fusion-evaporation reactions are ideally suited to the study of high-spin nuclear states [5, 41, 55]. This is the motivation for the ^7Li reaction, in which neutron evaporation should preferentially populate states at or near yrast [55]. Such states are likely to involve high- j orbitals, and be isomeric [5, 41], possibly facilitating study of the m2 isomer.

[‡] Production of ^{192}Ir with a ^{192}Os target requires exchange of one proton for one neutron. However, the literature does not seem to contain any precedent for such an exchange with a ^7Li projectile.

The experimental campaign concludes with the (p,n) reaction to investigate lower spin and angular momentum states. As a consequence of the p-n exchange, this reaction also produces isobaric analogue states of excited ^{192}Os , and may enable systematic comparison between the two nuclides. Whereas Hilgers and Tarkanyi did respectively perform the (p,n) and (d,2n) reactions, they did not collect, or, at least, did not report any significant gamma spectroscopic data [21, 22].

Predictive Simulations

In the absence of experimental data, predictive reaction simulation become necessary to estimate the excitation functions and reaction channel statistics, which inform projectile energy selection. Those relevant to this research include: *GNASH-D*, *EMPIRE-II*, and *PPACE*.

Excitation Function Data

F. Tarkanyi and K. Hilgers respectively report empirical excitation functions for the $^{192}\text{Os}(d,2n)^{192}\text{Ir}$ and $^{190}\text{Os}(p,n)^{192}\text{Ir}$ reactions. Figure 21 presents these data, which indicate a maximum cross section of about 400 mb at 12 MeV for the (d,2n) reaction, and about 65 mb at 10 MeV for the (p,n) reaction. However, available to the incident deuteron at 12 MeV is the (d,p) reaction channel, which results in the unwanted isotope ^{193}Os . Figure 21 lists the (d,2n), and (d,p) reaction data, which suggests the most favorable ratio of ^{192}Ir production to ^{192}Os production occurs between about 12 and 15 MeV, remaining roughly constant at 2.3. Clearly visible in the excitation function plots are the reaction threshold energies, which represent the difference between the Q -value and the Coulomb barrier.

Whereas none of the data sets include explicit measurements of the m2 isomeric ratio, the publications do report theoretical predictions for isomer production; these are also presented in Figure 21. Contributing to the predictions are the two reaction simulations *GNASH-D* and *EMPIRE-II*.

Note the literature does not contain any excitation function data for the (^7Li) reaction. While the *PPACE* reaction simulation code may facilitate predictions, it is likely the ideal kinetic energy must be determined through experiment. This is probably the case as well for m2 isomer production, using the other reactions.

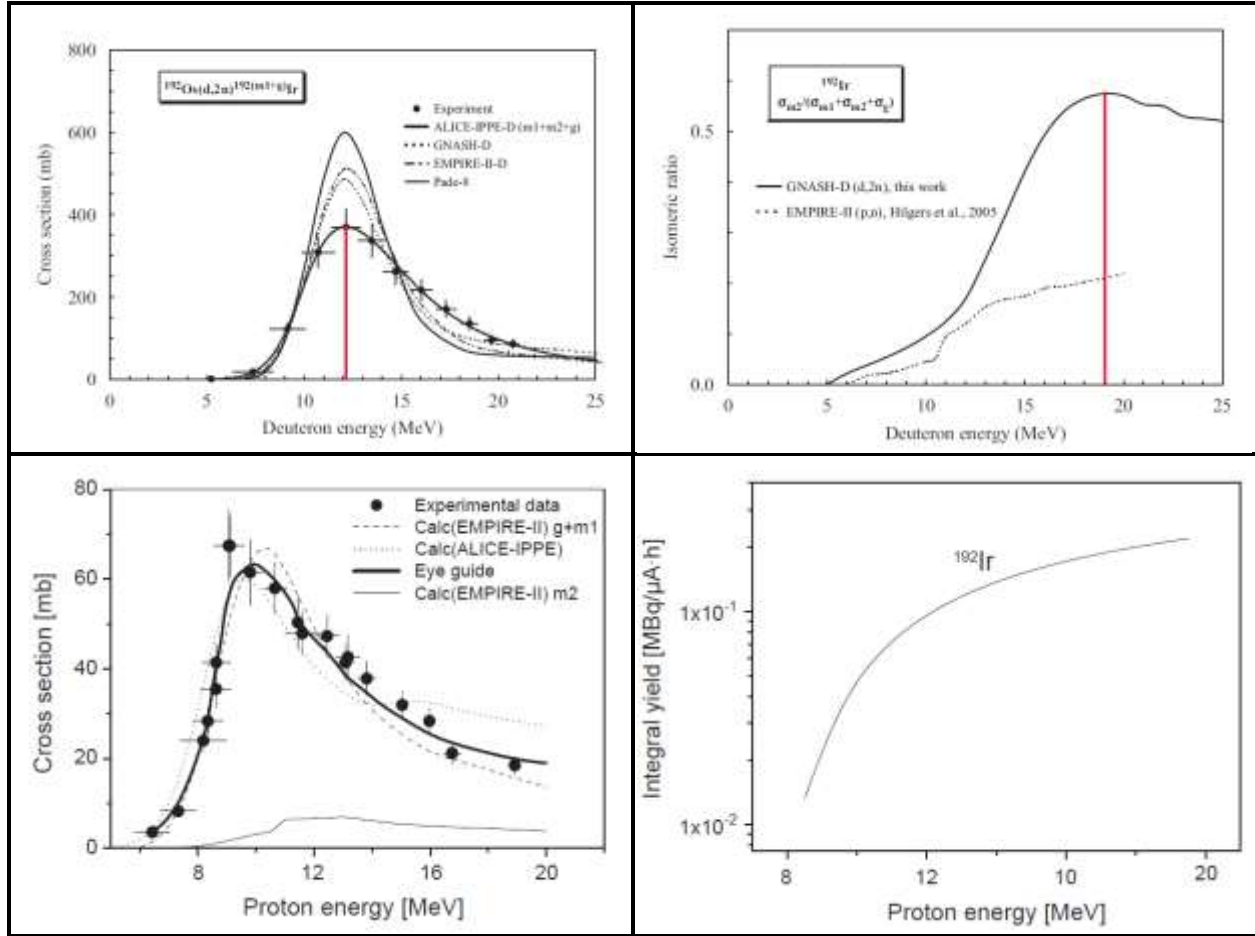



Figure 21. Empirical and theoretical excitation functions for the production of ^{192}Ir and the $^{192m2}\text{Ir}$ isomer. Upper left: $^{192}\text{Os}(d,2n)^{192}\text{Ir}$ excitation function from [21]. Upper right: model code predictions for $^{192m2}\text{Ir}$ isomeric ratio resulting from $^{192}\text{Os}(d,2n)^{192}\text{Ir}$ reaction from [21]. Lower left: $^{192}\text{Os}(p,n)^{192}\text{Ir}$ empirical and theoretical excitation functions; and theoretical m2 isomer excitation function. from [22]. Lower right: integral yield of the $^{192}\text{Os}(p,n)^{192}\text{Ir}$ reaction from [22].

Experimental Considerations

Determination of an appropriate kinetic energy for the reaction projectile requires consideration of several factors. Of course, the primary consideration is the level of nuclear excitation necessary to generate the desired data. This may be high in experiments exploring high angular momentum states and yrast cascades or low in nucleon capture experiments investigating non-selective statistical cascades. However, other factors may dictate projectile kinetic energies, which are suboptimal to the theoretically idyllic experiment. Figure 19 suggests a few of these considerations 

One must first recognize the projectile beam loses energy as it passes through the target material; it is therefore most beneficial to set the projectile energy such that the range of energy loss corresponds to the largest possible integrated cross section (area under the curve of the excitation function). However, the target thickness may also set an upper limit on the projectile energy, due to recoil of the products. If the energy is too great, the product nucleus Y may escape from the bulk target material, thus rendering its radiation potentially undetectable. Application of this constraint may necessitate a kinetic energy lower than that at the peak in the excitation function of Y . Complicating the tradeoff are other possible reaction channels, whose excitation functions may be significant or dominating in an energy region near the peak of Y . Moreover, the peak of an isomer excitation function does not in general align with the peak of the parent nucleus; so if isomer production is desirable the projectile energy decision must take this into account as well. For all practical purposes, a suitable balance of all factors may not be feasible, necessitating multiple experimental trials at different projectile energies.

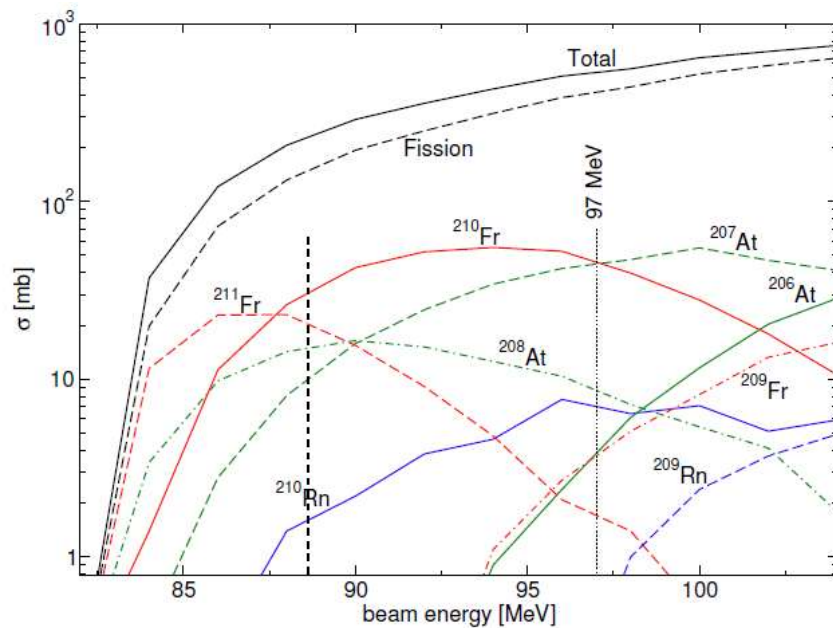


Figure 22. Plot of excitation functions for various products of a reaction. ^{210}Fr is the objective. The rightmost vertical line indicates the optimal projectile energy based on: (1) ^{210}Fr production relative to other nuclides; (2) the minimum target thickness, necessary to stop the recoiling ^{210}Fr nuclei; and (3), the energy loss (rightmost vertical line) of the projectile beam due to target transit. Total ^{210}Fr production is the area under the excitation function between the two vertical lines. Reproduced from [36]

Tradeoffs are evident in Figure 22, which depicts a plot of the excitation functions for competing reaction channels. In this case, the objectives are maximum production of ^{210}Fr , with minimum interference from competing channels. The optimal beam energy of 97 MeV (rightmost vertical


line), is then a consequence of (1) the target thickness, which is necessary to stop the recoiling product; and (2) the projectile energy loss (leftmost vertical line), due to projectile transit through the target.

Accelerator Equipment and Ion Beams

Indeed the projectile beam is a crucial component of the reaction experiments. Ideally the accelerator and associated equipment produce beams meeting all experimental requirements. Though not inclusive, the following beam properties are important for this research:

- Collimation and focus to maintain alignment of nuclei for possible angular correlation measurements
- Sufficient intensity to generate good statistics on coincidence correlations
- Sharp pulsing for lifetime measurements
- Well-defined and selectable energy, which can adjust to optimize proper nuclide output

14UD Tandem Accelerator

The 14UD Tandem Accelerator, at the Australian National University Heavy-Ion Accelerator Facility, serves as the source of the projectile beams for this campaign of experiments. Figure 23 schematically depicts the accelerator and the acceleration process. A product of the National Electrostatic Corporation, the 14UD is a pelletron accelerator, which operates at potentials exceeding  15MV. The projectile ions originate from a Source of Negative Ions by Cesium Sputtering (SNICS II), which uses a five kV anode to ionize cesium gas. The cesium ions then accelerate toward a cathode coated with the material comprising the projectile beam. Impacts of the cesium ions sputter the projectile material; whence projectiles travel through the cesium gas, acquiring an additional electron. A 150 kV potential accelerates the projectile ions for mass separation in a magnetic field.

Upon separation, a buncher uses a longitudinal, sinusoidal potential to form pulses of projectile ions, which then enter the primary accelerator. Three charging chains charge the 15 MV main terminal at the center of the accelerator structure. To minimize arcing, an annular pressure vessel, with SF₆ fill at six atmospheres, surrounds the central cavity, which contains the beam. Near the positive terminal, a thin carbon foil strips electrons from the projectile ions, changing

their charge from negative to positive. The direction of the acceleration thus remains constant and the projectiles continue to accelerate, reaching a final kinetic energy T , such that

$$T = V_0(1 + q) + T_0 \quad (148)$$

with terminal potential V_0 and projectile charge state q . A chopper, phase-matched to the beam pulse, subsequently eliminates the pulse tails and a second magnetic field selects the projectile energy corresponding to the desired charge state. The resulting beam energy uncertainty is approximately 0.1 to 0.3 percent. Throughout the acceleration process, a number of focusing elements also control the beam cross section, yielding a final diameter of about one millimeter for currents between one and ten nanoamps [58]. The range of beam energies and the collective set of controls ensure the 14UD accelerator meets the requirements for the proposed ^{192}Ir experiments; and it has seen use in related work [36, 59].

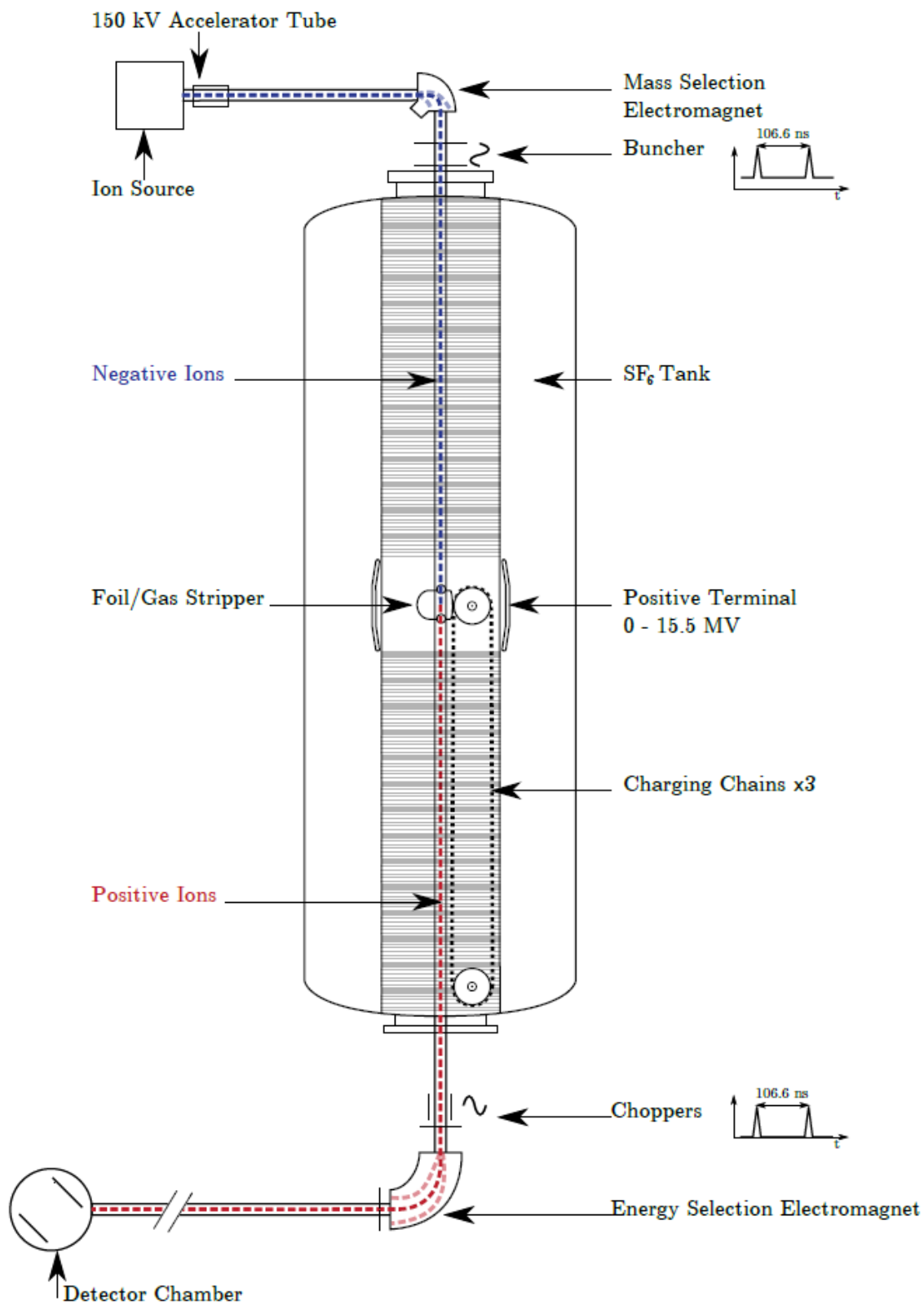


Figure 23. Schematic representations of the 14UD tandem accelerator and ion beam acceleration process.

Detectors

Of course, detection and measurement of the gamma radiation, which the decaying nucleus emits, represent the essence of these experiments. Most modern gamma detection systems rely on semiconductors, usually high-purity germanium (HPGe) or silicon, as primary detectors, which work in conjunction with scintillators for background suppression.

Semiconductor Detectors

Photons of ionizing radiation incident on the detector interact with the semiconductor material and, through the photoelectric absorption process, generate electron-vacancy (electron-hole) pairs. The number N of pairs depends on the energy E of the photon and the material ionization energy ϵ according to the relationship

$$N = E/\epsilon . \quad (149)$$

Subsequent collection of the “free” (conduction) charge, with a static electric field, results in a current or voltage pulse, whose amplitude is clearly proportional to the energy of the photon. It is this pulse, which constitutes the measurement.

At the interface of a p-type and n-type semiconductor, or p-n junction, a static electric field naturally develops by diffusion of majority charge carriers across the boundary. In the case of the p-type material, holes diffuse into the n-type material, leaving behind a stationary negative charge density; whereas the electrons in the n-type material diffuse into the p-type material, leaving a stationary positive charge density. Thus, the accumulations of positive space charge, on the n-type side, and negative space charge, on the p-type side, result in a potential gradient. Upon reaching sufficient magnitude, the gradient prevents further diffusion and the process comes to an equilibrium, whose width of space charge imbalance one calls the depletion region.

Ordinarily, in most junctions, the equilibrium contact potential and depletion region width are insufficient for charge collection in radiation detection applications [60]. However, under a reverse bias spanning the junction, the width of the depletion region increases; and nearly all of the applied voltage appears in the new equilibrium potential [60]. Neglecting derivation, one may express the width d of the depletion region under reverse bias V as

$$d \cong \left(\frac{2eV}{eN} \right)^{1/2}, \quad (150)$$

where e and N are respectively the electron charge and the net impurity concentration [60]. Importantly, maximization of usable detector volume requires the largest possible depletion region; and evidently this dependence extends to the material purity.

Spectral Resolution and Efficiency

Neglecting lifetime broadening (118), and after many detections, a gamma ray emitted from a specific, discrete transition ideally registers as a peak of infinitesimal width in an energy spectrum. However, detection artifacts, arising from charge collection statistics and noise, broaden an otherwise discrete peak into a distribution; and its energy is consequently uncertain. One typically quantifies this uncertainty as (1) the full width of the distribution at half maximum (FWHM), which has units of energy; or (2) as the unitless energy resolution R , according to

$$R = FWHM/H_0, \quad (151)$$

where H_0 is the peak centroid. As a consequence of an energy dependence to the FWHM, it is often favorable to use the latter

Detector efficiency generally refers to the probability of detection for an event of interest; in the case of semiconductor detectors, it is also an energy-dependent quantity. Given a number M of detections, which the detector registers in a particular time interval, one typically quantifies efficiency in two ways. Absolute efficiency ε_{abs} is the ratio of detections to source emissions.

$$\varepsilon_{abs} = M/M_s, \quad (152)$$

for number of source emissions M_s , during the time period of measurement. Intrinsic efficiency ε_{int} is the ratio of detections to source emissions incident on the detector.

$$\varepsilon_{int} = M/M_I, \quad (153)$$

for M_I incident emissions, which accounts for the detector solid angle and any attenuation along the path to the source. Specifically, with regard to detection of a particular gamma energy, one normally takes M to be the area of the peak in the spectrum and quotes the peak efficiency.

High-Purity Germanium

Compared to most other materials used for gamma spectroscopy, the superior energy resolution of HPGe makes it the material of choice for many modern detection systems [60]. However, due to its small, 0.7 eV bandgap, a thermally induced leakage current makes room temperature operation of germanium detectors impractical [60]. Cryogenic operation, usually at 77 K, and vacuum insulation from the surrounding air are therefore necessary.

A general expression for the energy resolution of an HPGe detector, given in terms of the FWHM W is

$$W_T^2 = W_D^2 + W_X^2 + W_E^2 . \quad (154)$$

The first term,

$$W_D^2 = 5.5225 F \epsilon E , \quad (155)$$

estimates the statistical fluctuation in the number of charge carriers as a function of gamma energy E and bandgap energy ϵ . The Fano factor F accounts for the variation between the observed variance and the Poisson predicted variance. In germanium, F typically ranges between 0.085 and 0.16 [60]. The two subsequent terms respectively represent the uncertainty contributions due to incomplete charge collection and electronic noise. One can determine the charge collection contribution, empirically, by measuring the FWHM as a function of voltage. An empirical determination of the noise is also possible by measuring the position of a peak from a pulser operating at known amplitude. All factors considered, energy resolution for HPGe detectors is nominally on the order of one to two percent [60].

One normally determines peak intrinsic efficiency of a germanium detector over a range of energy measurement through calibration. Typical calibration requires peppering the energy range with standard sources of known emissive activity and a good estimate of solid angle. For coaxial detectors of the type supporting these experiments, a common calibration function relates the logarithm of the efficiency f to the logarithm of the energy E according to

$$\ln f = \sum_{i=1}^N a_i \left(\ln \left(\frac{E}{E_0} \right) \right)^{i-1} , \quad (156)$$

where E_0 is a reference energy and the a_i are parameters of the fit. Figure 24 illustrates an example of such a fit. Note the peak near 100 keV, where photoelectric absorption becomes the dominant mode of ionizing radiation interaction in germanium.

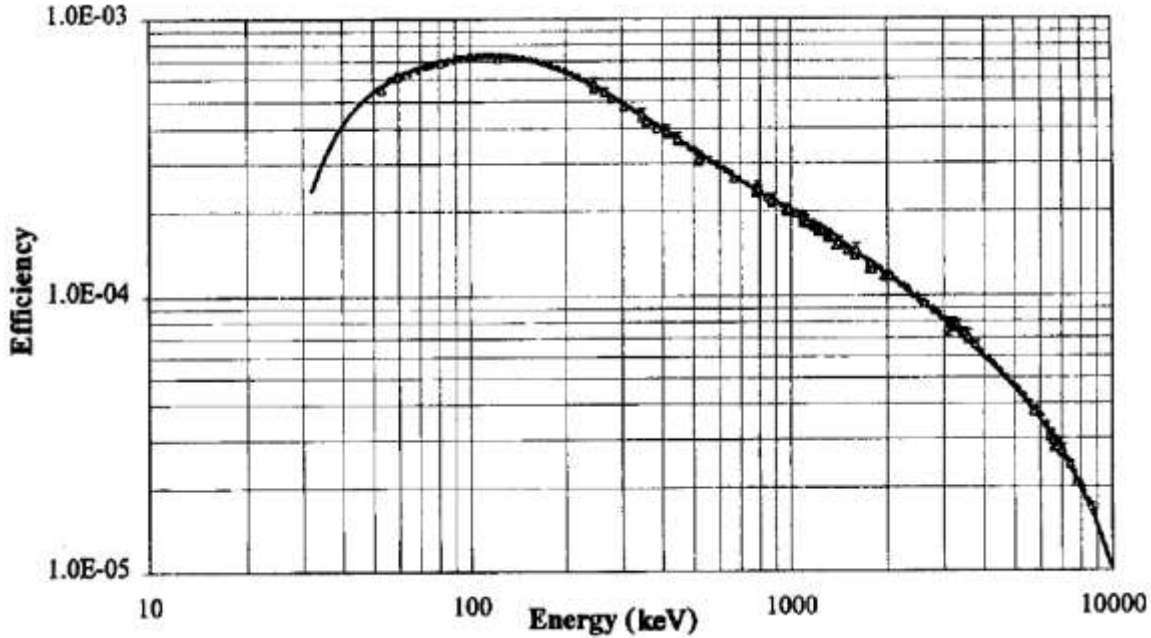


Figure 24. Sample calibration curve for an n-type detector. Reproduced from [60].

Low Energy Photon Spectrometer

Commonly, the detection material in LEPS detectors is lithium-drifted silicon Si(Li). In contrast to germanium, photoelectric absorption in silicon dominates other modes of interaction for photon energies below about 55 keV. Thus LEPS detectors tend to have higher efficiencies in the region of 1-50 keV, which may be particularly important for resolving transitions of closely-spaced nuclear levels. While cooling is not strictly necessary for silicon, cryogenic operation is common to maximize efficiency.

Computation of Si(Li) detector energy resolution is virtually identical to that of germanium, with uncertainty contributions from the same sources. Calibration is also similar to that of germanium, of course, with different standard sources and several possible empirical forms, such as,

$$f = a \exp(bE^c)(1 - \exp(dE^g)), \quad (157)$$

Where a , b , c , d , and g are parameters of the fit Figure 25. Illustrates a representative calibration curve for Si(Li).

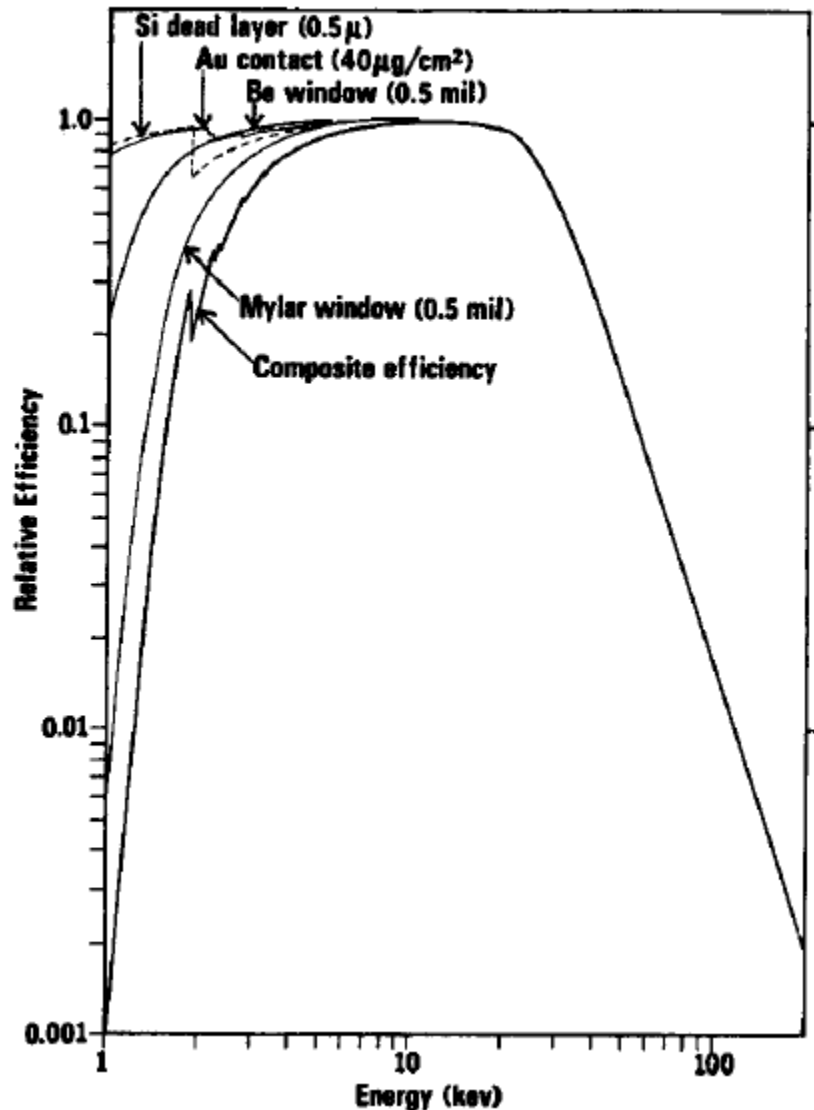


Figure 25. Representative efficiency calibration curves for Si(Li) detectors. From [knoll 481].

Background and Continuum Suppression

A dominant contribution to background in most spectra results from incident photons, which interact with detector electrons through a Compton scatter event, or at higher energies, a pair production event. Only at lower energies, in a given material, is photoelectric absorption the dominant interaction mechanism. Unlike photoelectric absorption, the other two interactions result in photons, which can escape the detector in lieu of depositing their full energy. In

particular, Compton scatter, which occurs over a continuum of energies, leaves behind a background continuum of partial energy events. Without any compensation, the background continuum might obscure true peaks of lower intensity.

One common approach to address the scattering problem is Compton rejection by anticoincidence. This technique employs a secondary detector, which surrounds the primary spectroscopic instrument. Rejection works by closing an electronic gate upon registration of an event in the secondary detector; and the electronic analysis system ignores any event pulses from the primary detector during gate closure. Events, which deposit their full energy in the primary detector obviously cannot interact with the secondary detector and are thus spared rejection. However, truly coincident events also can interact with each detector independently, triggering erroneous rejection. The resulting “false negative” can adversely affect counting statistics in spectroscopy of complex level schemes, where coincident events are numerous [60].

Normally the secondary detectors are composed of scintillator materials, such as bismuth germanate (BGO), which respond to ionizing radiation with emission of visible or infrared light. A photomultiplier tube then amplifies the optical signal and converts it to an electronic pulse. Although spectral resolution of scintillators is typically poor relative to HPGe, their detection efficiency is much higher. They are thus suitable for anticoincidence in Geiger mode operation, which registers only the presence of an event, at the expense of its spectral identity.

CAESAR Array

The Compton Suppressed Array (CSA or “CAESAR”), at the Australian National University Heavy-Ion Facility, is the primary detection system for these experiments. CAESAR is a gamma-ray spectroscopy array, consisting of eleven detectors, including nine Compton-suppressed, coaxial, n-type HPGe detectors and two unsuppressed low-energy photon spectrometer (LEPS) detectors [36]. Figure 26 is a schematic illustration of CAESAR, depicting the six HPGe detectors, which lie in the vertical plane at angles, as shown. The three hidden HPGe detectors lie out of the vertical plane, at angles of 49° , 53° , and 132° to the beam axis; whereas the two LEPS detectors, also hidden, lie out of the vertical plane at 70° and 135° to the beam axis. A bismuth germanate (BGO) scintillator detector sheaths each HPGe detector; and

the pair function in anticoincidence for Compton suppression. Absolute detection efficiency for the array is on the order of one percent [36].

To register ion beam pulses for gamma coincidence measurements, the CAESAR array electronics receive from the beam chopper, signals, which are some multiple of the beam pulse width. Coincidence timing electronics use these signals to measure gamma-ray detection times relative to the beam pulses; and this permits derivation of relative or coincidence times between gamma detections [36].

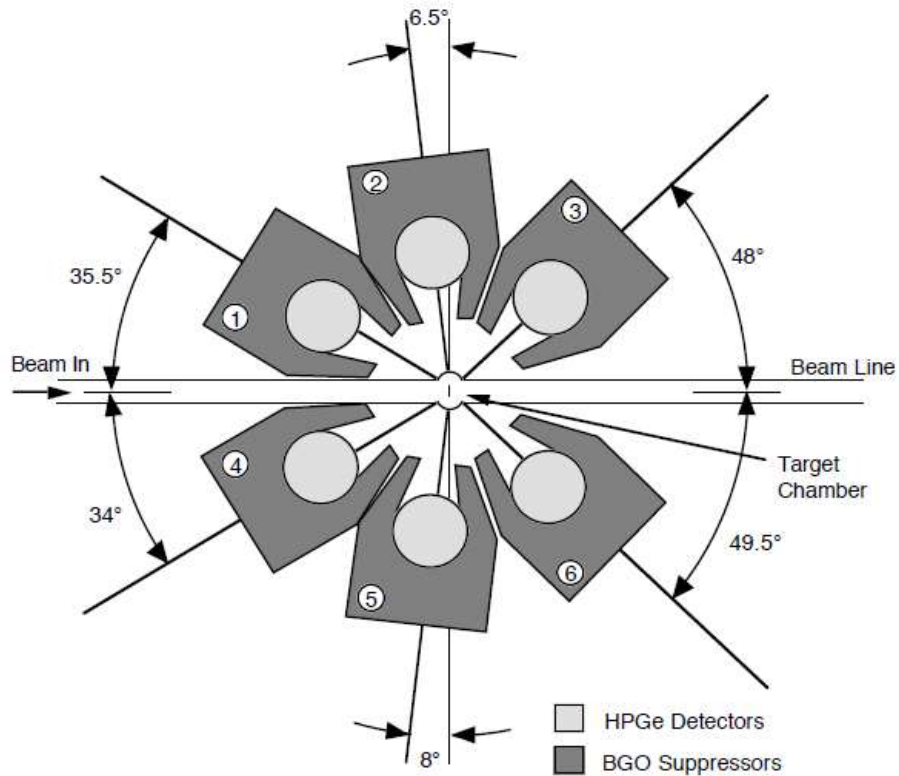


Figure 26. Schematic diagram of the CAESAR array for the six detectors in the vertical plane. Reproduced from [36]

V. Research Plan



Objectives

Explicit objectives of this research include:

- To the existing ^{192}Ir level scheme in the ENSDF, addition of transitions with spin-parity assignments, and phenomenological features of nuclear structure
- Confirmation of tentative transitions, spin-parity assignments, and phenomenological features
- Identification of feeding and decay pathways for the m2 isomer, to facilitate future experimentation and practical application

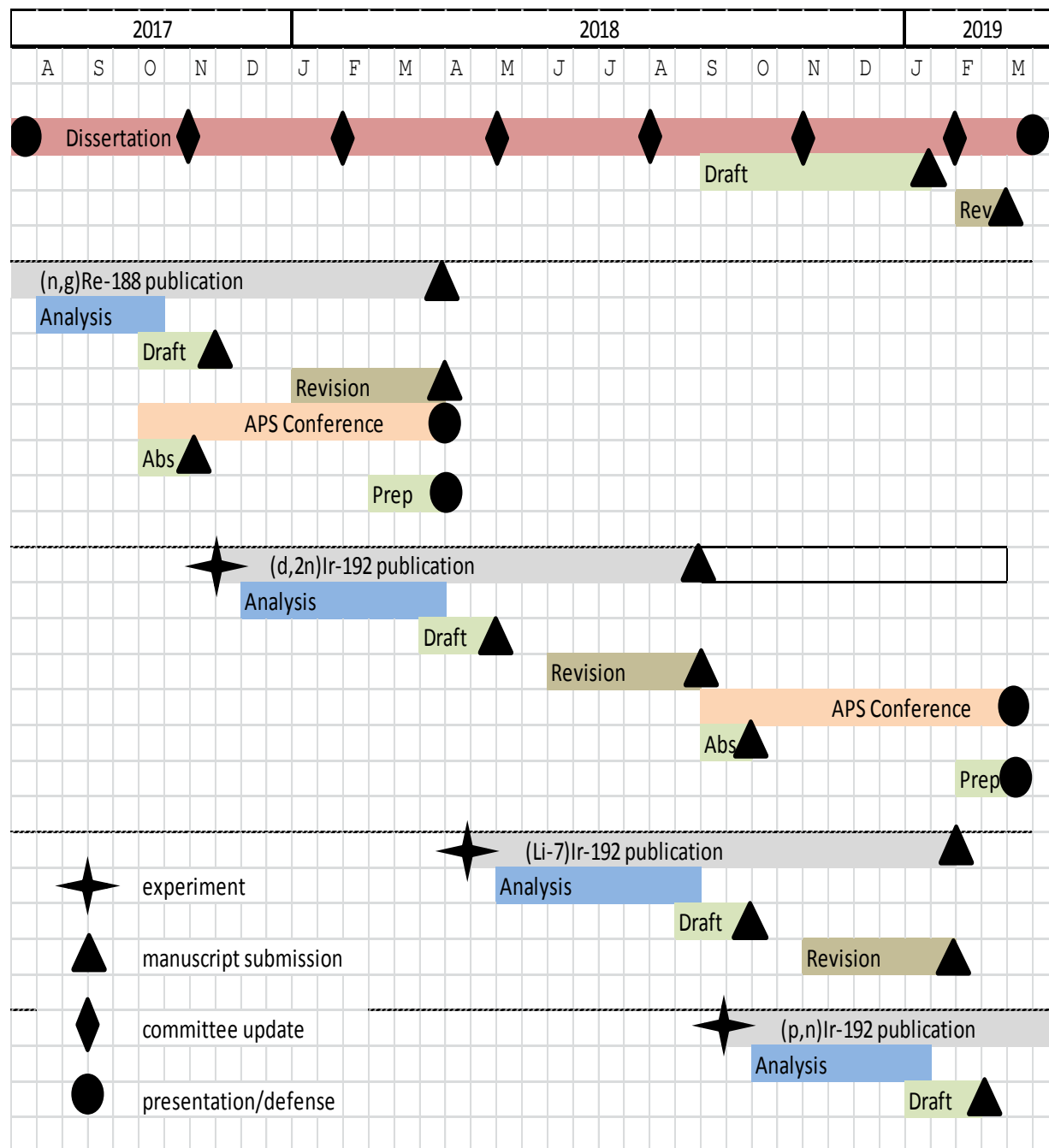
Chronology of Events

The research timetable is constructed under the assumptions of (1) a March 2019 dissertation defense and graduation, subsequent to completion of three to four unique analysis efforts; and (2) attendance at one to two APS conferences. There are a number of contingencies, including experiment execution timing and contributing author revisions, which add significant uncertainty to the proposed schedule; and some dynamic adjustment may be necessary.

- July 2017: Prospectus Defense
- August 2017: Candidacy
- August 2017: Re-188 analysis 
- October/November 2017: Re-188 abstract submission for spring APS meeting
- November 2017: Committee update
- November 2017: Draft Re-188 manuscript to coauthors
- November/December 2017: First  92 experiment
- December 2017: Begin first Ir-192 analysis and Re-188 coauthor revisions
- February 2018: Committee update
- February 2018: Begin preparation for spring 2018 APS meeting
- March/April 2018: Submit final draft of Re-188 manuscript to Phys Rev C for acceptance
- March/April 2018: Attend first APS conference to present Re-188 data
- April 2018: Second Ir-192 experiment
- May 2018: Committee update
- May 2018: Draft manuscript covering first Ir-192 experiment to coauthors
- May 2018: Analysis of second Ir-192 experiment data
- June 2018: Coauthor revisions to manuscript covering second Ir-192 experiment

- August 2018: Committee update
- August/September 2018: Draft manuscript covering second Ir-192 experiment to coauthors
- September 2018: Submit final draft of manuscript covering first Ir-192 experiment to Phys Rev C for acceptance
- September 2018: Begin draft of dissertation, with available analyses
- September 2018: Begin draft of abstract covering first Ir-192 experiment for submission to APS for spring 2019 meeting
- September/October: 2018: Third Ir-192 experiment
- October 2018: Draft manuscript covering second Ir-192 experiment to coauthors
- October 2018: Submit abstract covering first Ir-192 experiment to APS for spring 2019 meeting
- October 2018: Analysis of data from third Ir-192 experiment
- November 2018: Committee update
- November 2018: Coauthor revisions to manuscript covering second Ir-192 experiment
- January 2019: Begin draft of manuscript covering third Ir-192 experiment
- January 2019: Complete first draft of dissertation, with available analyses
- February 2019: Submit final draft of manuscript covering second Ir-192 experiment to Phys Rev C for acceptance
- February 2019: Committee update
- February 2019: Begin revisions to dissertation
- February 2019: Begin preparation for spring 2019 APS presentation
- February 2019: Draft manuscript covering third Ir-192 experiment to coauthors
- March 2019: Complete dissertation revisions
- March 2019: APS presentation covering first Ir-192 experiment
- March 2019: Dissertation Defense

Timetable



VII. References

1. C. Baglin, Evaluated Nuclear Structure Data File (ENSDF) for ^{192}Ir , NDS 113, 1871 (2012). Brookhaven National Laboratory. [Online]. Available: <http://www.nndc.bnl.gov/ensdf/>
2. P. Walker, “High-spin nuclear traps,” *Physics World*, February 1994.
3. M. Balodis et al. *EPJ Web of Conferences* 93, 01043 (2015)
4. “White Paper on Nuclear Data Needs and Capabilities for Basic Science,” U.S. Nuclear Data Program 2016
5. A. Jain, *Reviews of Modern Physics*, Vol. 70, No. 3, July 1998
6. M. Litz, “Controlled Extraction of Energy From Nuclear Isomers,” *Proceedings for the Army Science Conference*, December 2015
7. J. Carroll, *Laser Phys. Lett.* 1, No. 6, 275–281 (2004). DOI 10.1002/lapl.200310065
8. M. Balodis et al. *Nuclear Physics A* 933 (2015) 189–211
9. T. Bengtsson et al. *Nuclear Physics A* 436 (1985) 14-82
10. G. Lane, *Technical Supplement for Isomer and High-Spin Nuclear Research*, Australian National University. Submission to U.S. Army International Technology Center
11. G. Lane, “Nuclear structure of ^{192}Ir and search for isomer depletion levels,” Australian National University. White Paper submission to United States Army International Technology Center
12. Australian National University 14UD Pelletron, [Online]. Available: <https://physics.anu.edu.au/nuclear/14ud.php>
13. M. Gerathy et al. *EPJ Web of Conferences* 123, 04007 (2016). DOI: 10.1051/epjconf/201612304007
14. E. McMillan et al. *Phys. Rev.* 52, 375, August 1937
15. R. Robinson, *Atomic Data and Nuclear Data Tables* 98 (2012) 911–932
16. Nuclear Science References (NSR). Brookhaven National Laboratory. [Online]. Available: <http://www.nndc.bnl.gov/nsr/>
17. J. Kern et al. *Nuclear Physics A* 534 (1991) 77-127
18. P. Garrett et al. *Nuclear Physics A* 568 (1994) 445-498

19. M. Balodis et al. Proc.9th Intern.Symposium on Capture Gamma-Ray Spectroscopy and Related Topics. Vol.1, p.147 (1997)
20. J. Chen et al. Compiled (Unevaluated) Data for ^{192}Ir , Experimental Unevaluated Nuclear Data List (XUNDL). Brookhaven National Laboratory. [Online]. Available: <http://www.nndc.bnl.gov/ensdf/ensdf/xundl.jsp>
21. F. Tarkanyi et al. Applied Radiation and Isotopes 65, 1215–1220 (2007)
22. K. Hilgers et al. Applied Radiation and Isotopes 63, 93–98 (2005)
23. W. Doyle et al. Nuclear Physics 49, 449–455 (1963)
24. G. Audi et al. *Atomic Mass Evaluation 2011*, Priv. Comm. (2011)
25. G. von Weber et al. Z.Naturforsch., 8a, 580 (1953)
26. G. von Weber, Z.Naturforsch., 9a, 580 (1954)
27. R. Gehrke et al. Nucl.Instrum.Methods 97, 219 (1971)
28. J. Mize et al. Phys. Rev. 96, 444, (1954)
29. G. Scharff-Goldhaber, Phys. Rev. Lett. 3, 47 (1959)
30. G. Harbottle, Radiochim. Acta 13 (1970) 132.
31. NUDAT-2, Brookhaven National Laboratory. [Online]. Available: <http://www.nndc.bnl.gov/nudat2/getbandplot.jsp?unc=nds>
32. G. Scharff-Goldhaber, Bull. Am. Phys. Soc. 22, 545 (1977)
33. W. Greiner and J. A. Maruhn, *Nuclear Models*, Berlin-Heidelberg: Springer-Verlag, 1996.
34. R. F. Casten, *Nuclear Structure from a Simple Perspective*, 2nd ed. New York, NY: Oxford University Press, 2000.
35. K. S. Krane, *Introductory Nuclear Physics*. Hoboken, NJ: John Wiley & Sons, 1987.
36. V. Margerin, A thesis submitted for the degree of Master of Philosophy from the Australian National University, December, 2012
37. R. Bengtsson et al. Nature, Vol. 449, 411–413 (2007)
38. R. Woods et al. Phys. Rev. 95, 577 (1954)
39. M. Meyer, Phys. Rev. 74, 235 (1948)

40. R. L. Liboff, *Introductory Quantum Mechanics*, Third Edition. Addison-Wesley, 1998
41. P. Regan, *Post Graduate Nuclear Techniques*. (4NET) Course Notes. Department of Physics, University of Surrey, Guildford, UK, 2003
42. S. Nilsson and I. Ragnarsson, *Shapes and Shells in Nuclear Structure*. New York, NY: Cambridge University Press, 2005
43. R Lieder et al. Adv. in Nucl. Phys. 10, 1 (1978)
44. A. Jain et al. Phys. Lett. B 209, 19 (1988)
45. . A. Jain et al. Phys. Rev. C 40, 432 (1989)
46. C. Gallagher, Phys. Rev. 111, 1282 (1958)
47. N. Newby Phys. Rev. 125, 2036 (1962)
48. P. Boisson et al. Phys. Rep. 26, 99 (1976)
49. P. Sood et al. Nucl. Phys. A 373, 519 (1982)
50. P. Prokofjevs et al. Phys. Rev. C 61, 044305 (2000)
51. F. Kondev et al. Atomic Data and Nuclear Data Tables 50, 103-104 (2015)
52. G. Alaga, Phys. Rev. 100, 432 (1955)
53. K. Löbner, Phys. Lett B 26, 341-412 (1968)
54. G. Alaga et al. Nucl. Phys A 4, 625 (1957)
55. J. Newton, "Gamma Rays from Heavy Ion Reactions," *Nuclear Spectroscopy and Reactions* Part C, Comp. by J. Cerny. New York, NY: Academic Press, 1974
56. F. Stephens, Nucl. Phys. A183, 257 (1972)
57. A. Jain, Nuclear Data Sheets 128, 1–130 (2015)
58. K. Cook, A thesis submitted for the degree of Doctor of Philosophy from the Australian National University, December, 2016
59. D. Matters, A thesis submitted for the degree of Doctor of Philosophy from the U.S. Air Force Institute of Technology, December, 2016
60. G. Knoll, *Radiation Detection and Measurement* 4th Ed. Danvers, MA: John Wiley & Sons, 2010

61. D. Radford, *RadWare*, Oak Ridge National Laboratory. [Online]. Available: <http://radware.phy.ornl.gov/>